ANNUAL REVIEWS

Annual Review of Astronomy and Astrophysics

Magnetohydrodynamic Waves in the Solar Corona

Valery M. Nakariakov[1,2,3] and Dmitrii Y. Kolotkov[1,4]

[1]Centre for Fusion, Space and Astrophysics, Physics Department, University of Warwick, Coventry CV4 7AL, United Kingdom; email: V.Nakariakov@warwick.ac.uk

[2]School of Space Research, Kyung Hee University, Yongin, 446-701, Korea

[3]St. Petersburg Branch, Special Astrophysical Observatory, Russian Academy of Sciences, 196140 St. Petersburg, Russia

[4]Institute of Solar-Terrestrial Physics, Siberian Branch of Russian Academy of Sciences, Irkutsk 664033, Russia

Annu. Rev. Astron. Astrophys. 2020. 58:441–81

First published as a Review in Advance on July 14, 2020

The *Annual Review of Astronomy and Astrophysics* is online at astro.annualreviews.org

https://doi.org/10.1146/annurev-astro-032320-042940

Keywords

Sun: corona, Sun: oscillations, waves

Abstract

The corona of the Sun is a unique environment in which magnetohydrodynamic (MHD) waves, one of the fundamental processes of plasma astrophysics, are open to a direct study. There is striking progress in both observational and theoretical research of MHD wave processes in the corona, with the main recent achievements summarized as follows:

- Both periods and wavelengths of the principal MHD modes of coronal plasma structures, such as kink, slow and sausage modes, are confidently resolved.
- Scalings of various parameters of detected waves and waveguiding plasma structures allow for the validation of theoretical models. In particular, kink oscillation period scales linearly with the length of the oscillating coronal loop, clearly indicating that they are eigenmodes of the loop. Damping of decaying kink and standing slow oscillations depends on the oscillation amplitudes, demonstrating the importance of nonlinear damping.
- The dominant excitation mechanism for decaying kink oscillations is associated with magnetized plasma eruptions. Propagating slow waves are caused by the leakage of chromospheric oscillations. Fast wave trains could be formed by waveguide dispersion.

- The knowledge gained in the study of coronal MHD waves provides ground for seismological probing of coronal plasma parameters, such as the Alfvén speed, the magnetic field and its topology, stratification, temperature, fine structuring, polytropic index, and transport coefficients.

Contents

1. INTRODUCTION

The outermost layer of the atmosphere of the Sun, the corona, is a fully ionized plasma penetrated by the magnetic field emerging through the solar surface. Typical temperatures of the coronal plasma range from ~1 MK in the quiet regions to several tens of millions of Kelvin in flaring structures. Typical values of the plasma concentration in the lower corona are about 10^9–10^{10} cm^{-3} in active regions, reaching 10^{12} cm^{-3} in flaring loops and decreasing to 10^8 cm^{-3} in coronal holes. The density of the coronal plasma decreases with height because of the gravity. A typical value of the density stratification scale height is ~50 Mm for the temperature of 1 MK. The magnetic field

CORONAL LOOPS

Coronal loops are magnetic flux tubes that begin and end at the surface of the Sun. A loop is usually filled in with a plasma that is denser and hotter than the surrounding plasma. Footpoints of the loops are embedded in a much denser plasma of the solar surface and are, hence, line-tied. Loops are a key building block of the closed corona.

reaches several hundred Gauss above sunspots, whereas it is several tens of Gauss in active region loops and several Gauss in the diffuse corona and coronal holes, and then rapidly drops down with the height. In the corona, the plasma parameter β, which is the ratio of the gas to magnetic pressures, is typically lower than unity. However, much higher values of β are reached in the lower layers of the solar atmosphere, i.e., the chromosphere and photosphere. Throughout this review, the low β condition is always assumed. Some magnetic field lines begin at the solar surface and go to the heliosphere, constituting a so-called open corona, whereas some others return back to the solar surface, forming loop-like structures. Coronal regions in which magnetic field lines return to the solar surface without reaching heliospheric heights are known as the closed corona. The locally open coronal regions are usually associated with coronal holes that are radially extended regions with the magnetic field stretched predominantly outward from the Sun. The high temperature and low density of the corona make it difficult to observe the coronal plasma in visible light. Hence, the corona is mainly studied in extreme-UV (EUV), soft X-ray, and radio/microwave bands; the forbidden lines in the optical band are used too. At the heights above ~1/3 of the solar radius, the corona can be studied in the white light scattered by free electrons.

The observations show that the corona is a highly nonuniform medium with a number of distinct plasma structures. Some magnetic flux tubes are filled in with a dense plasma, forming loops in the closed corona [known as coronal loops (see the sidebar titled Coronal Loops); see also Reale 2014 for a review], and bright plumes (see the sidebar titled Plumes) in the open corona (Wang 2009). The density contrast inside and outside loops and plumes is usually from ~3 to ~10, reaching 100 or more in flaring loops. Typical major radii (i.e., the radii of curvature) of coronal loops are from a few tens to a few hundred million meters, reaching in transequatorial loops about the radius of the Sun. For reference, a typical value of the electron mean-free-path distance is ~100 km for the temperature of 1 MK and concentration of 10^9 cm^{-3} (e.g., Peter 2015). The observationally estimated minor radii of loops are ~1 Mm, which is comparable with the pixel sizes of modern imaging EUV telescopes. For example, the pixel size of the Atmospheric Imaging Assembly on the *Solar Dynamics Observatory* (SDO/AIA) corresponds to ~400 km on the Sun. However, there are models that consider individual loops as bunches of even thinner, unresolved threads with the radii of several tens of kilometers. In observations, the loops are usually seen to be planar, meaning that the magnetic field there is not likely to be strongly writhed and twisted. The critical value of the twist, corresponding to the kink instability, is a bit more than one full rotation (2.5π) around the loop's axis. Polar plumes have a radial extent up to several solar radii and a width of several tens of millions of meters near the bottom. It is not known whether plumes have a fine structure and whether they have a magnetic twist.

SDO/AIA: the Atmospheric Imaging Assembly instrument on NASA's *Solar Dynamics Observatory*

PLUMES

Plumes are spatially confined and unipolar ray-like plasma structures directed radially outward from the Sun. Plumes are usually cooler and denser than the surrounding interplume regions.

MAGNETOHYDRODYNAMICS

Magnetohydrodynamics is a mathematical model that describes macroscopic (large-scale, slow, and long-durational) processes in a plasma in terms of partial differential equations consisting of the fluid mechanics and electromagnetism equations.

The corona is a highly dynamic medium that shows a manifold of physical phenomena. Typical lifetimes of individual loops are a few hours, whereas their bundles and active regions, as well as coronal holes, may be observed for several days or even weeks. Other important manifestations of coronal activity are impulsive energy releases, such as solar flares and coronal mass ejections (see, e.g., Chen 2011 for a review). Flares and mass ejections are subject to intensive studies in the context of space weather. Forecasting of extreme events of space weather requires detailed knowledge of physical parameters in their epicenters and deep insight into the basic processes operating there.

On shorter timescales, there are various transient phenomena, such as jets and small eruptions, and oscillations and waves, which are the subjects of this review. Typical wavelengths of wave processes detected in the corona range from a few million to several hundred million meters and typical periods from subseconds to several tens of minutes. By the order of magnitude, those timescales are consistent with the sound, Alfvén, and fast timescales[1] in typical plasma nonuniformities, e.g., coronal loops. Furthermore, high-precision observational tools allow us to resolve, in a number of cases, both wave period and wavelength simultaneously, giving the estimations of the instantaneous phase speed of the wave. Typical phase speeds of propagating coronal waves range from a few tens to a few thousand kilometers per second, which is consistent with theoretically estimated values of the sound, Alfvén, and fast speeds in the coronal plasma (see Section 2 for details). This indicates that the wave and oscillatory processes observed in the corona are of a magnetohydrodynamic (MHD; see the sidebar titled Magnetohydrodynamics) nature. In addition, the collisional nature of the coronal plasma is consistent with the applicability of the MHD approach to the wave motions with parallel wavelengths greater than 1 Mm. In the perpendicular direction, MHD is adequate for even much shorter wavelengths.

The intrinsically structured nature of the coronal plasma, highly filamented along the tangled magnetic field, allows for the existence of various MHD waveguides and resonators (e.g., Roberts 2000). The magnetic structuring of the coronal plasma determines the main properties of solar coronal waves and oscillations. In particular, the nonuniformity causes geometrical dispersion and mode coupling, which can significantly affect the wave dynamics. Almost always, the observed waves are associated with certain plasma structures, e.g., specific loops, plumes, streamers, and jets. In other words, coronal MHD waves are usually of the local nature. The exception is a so-called EIT wave that is observed by the Extreme-ultraviolet Imaging Telescope (EIT) to propagate outward from an energy release site, and may affect almost the whole solar disk. In this review, this phenomenon is not discussed, and the interested reader is referred to Long et al. (2017).

MHD waves have been intensively studied in various natural and laboratory plasma environments, in particular in Earth's magnetosphere, solar wind, and thermonuclear fusion reactors, for several decades. However, the corona offers the researchers a natural laboratory for the comprehensive investigation of omnipresent MHD waves that are well resolved simultaneously in time and space. Obviously, in the corona it is impossible to control experimental conditions, as they

[1]The sound, Alfvén, and fast timescales are travel times at a certain distance at the sound, Alfvén, and fast speeds, respectively.

could be in a laboratory plasma, but the corona offers a broad variety of combinations of different physical parameters of the plasma objects that host MHD waves. Thus, coronal wave studies have direct implications for MHD waves in other plasma environments, for example, in controlled fusion, geophysics, and astrophysics. In the context of MHD wave dynamics, the essential properties of the corona are the pronounced field-aligned filamentation of the plasma in density and temperature, coexistence of the regions of the locally open and closed magnetic field, and the possibility of the collisional regime. Another, recently understood feature of the corona is its ability to behave as an active medium, in which the waves could gain energy from, for example, the energy supply mechanism responsible for the plasma heating.

The interest in waves detected and theoretically predicted in the corona is connected with several important problems of modern solar physics and plasma astrophysics. First of all, the corona is a plasma environment allowing for a thorough study of a fully ionized, magnetically dominated plasma. In particular, MHD waves detected in the corona are possibly the longest MHD and, hence, electromagnetic waves in the Universe, resolved simultaneously in time and space. A highly debated topic is a possible role of MHD waves in the enigmatic problems of heating of the solar and stellar coronae and acceleration of the solar and stellar winds. Waves could carry the energy through different layers of the solar atmosphere and deposit it in the corona by some as-yet-unidentified but intensively investigated dissipative processes (see, e.g., Liu & Ofman 2014, Arregui 2015, Klimchuk 2015, Ofman 2016, Cranmer & Winebarger 2019, for recent reviews). The main question is whether the energy carried by observed waves is sufficient to compensate for the energy losses by optically thin radiation and thermal conduction to the chromosphere (e.g., De Moortel & Browning 2015). In addition, MHD waves could trigger impulsive energy release phenomena of flares and coronal mass ejections (e.g., Nakariakov et al. 2006), and, in particular, produce quasi-periodic modulation of the flaring emission (e.g., Van Doorsselaere et al. 2016). Furthermore, the generation of MHD waves acts as an additional sink of the released magnetic energy. The latter issue is rather natural, as an impulsive and spatially localized energy deposition in an elastic and compressible medium such as the corona should result in the excitation of waves propagating outwardly from the epicenter. MHD waves excited by flares can spread the released energy and the associated heating at a certain distance around the energy release site, in particular, across the field. However, the efficiency of this process needs to be assessed; some evidence of this has been found in observations (Huang et al. 2018). In addition, the waves excited by flares could reach another potentially flaring magnetic structure and trigger the energy release there. It may lead to chains of consecutive flares appearing at different spatial locations, known as sympathetic flares (e.g., Moon et al. 2002), or be responsible for the observed progression of elementary energy releases along the magnetic neutral line in major, two-ribbon flares (Nakariakov & Zimovets 2011). Another rapidly developing research direction is the diagnostics of coronal plasmas by MHD waves, i.e., the method of MHD seismology. As properties of MHD waves depend on properties of the plasma environment that supports them, it becomes possible to use the waves for probing macroscopic parameters of the plasma in the vicinity of the wave propagation region.

In the late 1990s, high-resolution space-borne EUV imagers and spectrometers as well as ground-based facilities (e.g., radioheliographs) started providing well-documented detection of MHD waves in the solar corona; this has become one of the most rapidly developing and fashionable research topics. The evolution of our understanding of coronal wave and oscillatory phenomena and competing interpretations and points of view can be traced by a series of comprehensive reviews (e.g., Roberts 2000, Nakariakov & Verwichte 2005, Aschwanden 2006, De Moortel & Nakariakov 2012, Liu & Ofman 2014, Wang 2016) and the topical issue of *Space Science Reviews*, Volume 149 (see Nakariakov & Erdélyi 2009). A neighboring, closely related research field is the study of oscillations in solar prominences (e.g., Arregui et al. 2012). Comparison of the MHD wave

behavior in the corona and Earth's magnetosphere, highlighting certain differences and similarities, can be found in Nakariakov et al. (2016b).

Total pressure: a sum of the thermodynamic pressure and the magnetic pressure in the plasma in MHD

Mode: a collective natural, or eigen oscillation of a dynamical system

In this review, we highlight the recent progress in observational studies and theoretical modeling of MHD waves in the solar corona and the use of wave observations in the seismological probing of the corona. Comprehensive recent reviews of wave processes in other parts of the solar atmosphere, e.g., in the chromosphere, can be found elsewhere (e.g., Jess et al. 2015). As the format of this review does not allow us to even mention several hundred research papers published in the field in the past ten years, the choice of the section topics reflects the authors' personal views.

2. THEORETICAL MODELING OF MAGNETOHYDRODYNAMIC WAVES IN PLASMA STRUCTURES OF THE CORONA

The standard theoretical approach that is used in the interpretation of coronal wave and oscillatory processes is the model of linear MHD oscillations of a plasma cylinder, developed by Zajtsev & Stepanov (1975) and Edwin & Roberts (1983). Such a cylinder could be considered as an elementary building block of the coronal plasma, representing various field-aligned plasma nonuniformities observed in the corona, such as loops, plumes, plasma jets, and various filaments. Despite the existence of alternative models, for example, based on a magnetic arcade (e.g., Hindman & Jain 2014), the plasma cylinder model and a connected slab model remain the standard theoretical approaches. The cylinder model led to the theoretical prediction of the waves that are now routinely detected in the corona and provided grounds for a number of generalizations, as well as the terminology used by the coronal wave research community.

In the simplest and most commonly used version of this model, the magnetic field inside and outside the cylinder is taken to be parallel to the cylinder's axis. Parameters of the plasma, such as the density and temperature, and the magnetic field are taken to depend on the radial coordinate only. The equilibrium condition requires the total pressure to be constant everywhere. If the equilibrium plasma quantities are constant inside and outside the cylinder but experience jumps at the boundary of the cylinder, one can solve linearized MHD equations inside and outside the cylinder and apply certain boundary conditions at the axis and at infinity. In addition, the internal and external solutions should be matched at the boundary to satisfy the continuity of the total pressure perturbations and radial displacement. The condition of the existence of the nontrivial solution gives dispersion relations that link the oscillation frequency of a specific mode with the parallel (axial) wavelength; the azimuthal wave number, m; and the equilibrium parameters. Solutions of linearized MHD equations provide us with the radial structure of the perturbations of the plasma density, temperature, and pressure; the magnetic field; and the velocity and displacement vectors. A detailed description of this procedure, as well as dispersion relations, is provided in several previous reviews of this topic (e.g., Nakariakov & Verwichte 2005).

As the considered system has a natural spatial scale (i.e., the radius of the cylinder, a), MHD modes are dispersive. In other words, their properties, in particular, characteristic speeds and the radial structure of the perturbation, depend on the frequency or parallel wave number, $k_\parallel$. In addition, properties of MHD perturbations are determined by the sound (C_s) and Alfvén (C_A) speeds inside and outside the cylinder and the azimuthal wave number, m. As m is an integer, it provides us with a useful starting point for the classification of different MHD modes of the plasma cylinder, in particular of the sausage, $m = 0$, and kink, $m = \pm 1$, types (see Sections 2.1–2.3 and **Supplemental Figures 1** and **2** of the **Supplemental Text**). The radial structure of the perturbations inside the cylinder is given by a Bessel function of an integer order determined by m (see **Supplemental Figure 3** of the **Supplemental Text**). Different boundary conditions

Supplemental Material >

at infinity allow one to consider trapped and leaky regimes.[2] In the trapped regime, the radial structure of the perturbation outside the cylinder is described by a MacDonald function; i.e., the wave perturbation decreases with the radial distance superexponentially, as $r^{-1/2}\exp(-r)$. The characteristic distance of the extent of a trapped oscillation in the external medium, $r_{\rm ex}$, could be estimated as

$$r_{\rm ex} = \left[\frac{(C_{\rm se}^2 + C_{\rm A_e}^2)(C_{\rm Te}^2 - V_{\rm ph}^2)}{(V_{\rm ph}^2 - C_{\rm se}^2)(V_{\rm ph}^2 - C_{\rm A_e}^2)}\right]^{1/2} \frac{1}{k_\parallel}, \qquad 1.$$

where $V_{\rm ph} = \omega/k_\parallel$ is the phase speed[3] along the cylinder. In the leaky regime, the radial structure of the perturbation is given by a Hankel function. As the outward propagating wave is cylindrical, its amplitude decays as $r^{-1/2}$. In both leaky and trapped regimes, the cylinder acts as an MHD waveguide, directing both fast and slow magnetoacoustic waves along the magnetic field. In a low-β plasma, properties of the fast and slow magnetoacoustic waves modified by the cylinder, i.e., fast and slow modes, respectively, are rather different. In addition to MHD modes, the cylinder supports a continuum of torsional Alfvén waves that make alternate rotational motions accompanied by alternate twisting of the field. The radial structure of torsional waves is arbitrary. At different azimuthal shells in the cylinder, torsional waves propagate at local Alfvén speeds and are independent of torsional waves of neighboring shells. Torsional waves are not collective modes.

Typically, the plasma density in a coronal waveguiding nonuniformity is higher than that outside of it. Hence, in a low-β plasma the Alfvén speed inside the cylinder, $C_{\rm A_i}$, is lower than the Alfvén speed outside it, $C_{\rm A_e}$. Phase speeds of fast modes are situated between those two values. In the zero-β limit, the effective radial wave number of fast perturbations is $\kappa_{\rm r} = [\omega^2/C_{\rm A}^2(r) - k_\parallel^2]^{1/2}$, with the phase speed $V_{\rm ph}$ determined by the whole radial profile of $C_{\rm A}$. Consequently, in the regions in which $V_{\rm ph} > C_{\rm A}$, the radial structure of the fast perturbations is oscillatory, whereas in $V_{\rm ph} < C_{\rm A}$ it is either growing or decaying monotonically.

The former regions act as waveguiding cavities for fast waves. In the long parallel-wavelength limit, all fast modes except $m = 0$ approach the kink speed,[4] $C_{\rm K}$, and are trapped for all values of $k_\parallel$. Slow waves are weakly sensitive to the plasma conditions outside the cylinder, and their phase speeds have values between the internal sound speed, $C_{\rm si}$, and the tube speed,[5] $C_{\rm Ti}$. Slow waves are also trapped for all $k_\parallel$. In addition to m, specific modes are identified by the radial mode number, $n_{\rm R}$, which is the number of nodes of the radial velocity induced by the wave in the radial direction. Fast modes with high $n_{\rm R}$ are leaky.

Standing modes appear if one applies boundary conditions at different locations along the cylinder. In particular, it could be the line-tying or reflecting conditions at the footpoints of a coronal loop. Standing modes are characterized by a triplet of mode numbers: m, $n_{\rm R}$, and also the

[2] In the trapped regime, wave perturbations outside the cylinder are exponentially evanescent; i.e., the internal perturbation experiences a total internal reflection at the boundary of the cylinder. In the leaky regime, the waves propagate outward from the cylinder; i.e., the cylinder acts as a fast magnetoacoustic antenna.

[3] Phase speeds of guided waves are defined in the direction of the waveguide, i.e., in the parallel (axial) direction in the discussed geometry. The group velocity is in the parallel direction too. However, the local, instantaneous phase velocity could be highly oblique.

[4] Kink speed is the phase and group speeds of all fast modes with $m > 0$ in the long-wavelength limit, defined as $C_{\rm K} = \left(\frac{\rho_{\rm i} C_{\rm A_i}^2 + \rho_{\rm e} C_{\rm A_e}^2}{\rho_{\rm i} + \rho_{\rm e}}\right)^{1/2}$, where ρ is the equilibrium plasma density, and the indices "i" and "e" denote the quantities inside and outside the cylinder.

[5] Tube speed is the speed of a slow mode in the long-wavelength limit, defined as $C_{\rm T} = \frac{C_{\rm A} C_{\rm s}}{\sqrt{C_{\rm A}^2 + C_{\rm s}^2}}$. The tube speed is lower than both Alfvén and sound speeds, approaching the sound speed in the zero-β limit.

OSCILLATION QUALITY FACTOR

Oscillation quality factor (q-factor) is a dimensionless parameter, determined by the ratio of the decay time (length) to the oscillation period (wavelength). It characterizes the number of oscillation cycles within which the wave amplitude decreases to a certain relative value.

parallel mode number, n_L, which is the number of antinodes in the perturbation of the velocity along the cylinder.

Recently, attention has been paid to the modeling of the observational manifestation of MHD modes of various coronal plasma structures in the data of specific instruments, i.e., forward modeling of observables (e.g., Van Doorsselaere et al. 2016). It accounts for the effects of the integration along the line of sight (LoS), the size of the pixel or the beam size, either specific atomic transitions in the bandpass of interest (e.g., in the EUV band) or specific emission mechanisms (in the microwave band), and instrumental response functions.

2.1. Sausage Modes

Sausage modes are axisymmetric, $m = 0$, fast magnetoacoustic perturbations of the plasma cylinder. In the low-β plasma, they are characterized by predominantly radial flows. In a cylinder with the step-function radial density profile, in the long wavelength limit, sausage modes with all n_R are leaky; i.e., the local incidence angle exceeds the threshold of the total internal reflection. In this limit, the period of standing sausage oscillations is independent of the parallel wavelength and can be estimated as $P_{saus} \approx 2\pi a/(\eta_{n_R} C_{A_i})$, where η_{n_R} is the n_R-th zero of the Bessel function J_0 (e.g., Kopylova et al. 2007). The oscillation quality factor (q-factor; see the sidebar titled Oscillation Quality Factor) is $\tau_D^{(leak)}/P_{saus} \approx \pi^{-2}(\rho_i/\rho_e)$, where $\tau_D^{(leak)}$ is the damping time (see the sidebar titled Damping Time) because of the wave leakage. Thus, in the loops having density contrast ρ_i/ρ_e lower than 10, long-wavelength sausage waves get damped in shorter than one cycle of the oscillation, whereas in denser loops the leaky oscillations can last long enough for their detection. Comprehensive analysis of the effect of the leakage in the vicinity of the cutoff has been performed by Vasheghani Farahani et al. (2014). However, sausage modes of shorter wavelength, including standing oscillations typical of the short and dense loops in solar flares, are in the trapped regime. In this regime, the sausage oscillation period depends on the parallel wavelength, $P_{saus} \approx 2\pi/(k_\parallel C_{A_e})$ (e.g., Nakariakov et al. 2012). With the increase in $k_\parallel$, the speed in the denominator decreases to C_{A_i}. In both regimes, the phase speed decreases rapidly with the increase in $k_\parallel$; i.e., sausage modes are highly dispersive.

Properties of sausage oscillations were found to be dependent on the steepness of the radial density profile (Nakariakov et al. 2012, Chen et al. 2015a). The difference in the sausage periods between cylinders with a Gaussian and step-function radial profiles is more than a factor of two. More generally, with the use of the oscillatory theorem, Lopin & Nagorny (2015, 2019) showed

DAMPING TIME

Damping time (length) is a characteristic time (distance) of the wave amplitude decrease. Usually, it is used for the indication of the e-folding time or distance. However, other damping laws, e.g., Gaussian damping, may occur.

that sausage modes are in the trapped regime for all $k_\parallel$, if $r^2\rho(r) \to \infty$ at $r \to \infty$. If this condition is not fulfilled, sausage modes could be in both leaky (for small $k_\parallel$) and trapped regimes. The increase in the density profile steepness leads to an increase in the wave dispersion, i.e., in $dV_{ph}/dk_\parallel$. Pascoe et al. (2009) addressed the effect of fine transverse structuring of the equilibrium density on sausage oscillations, modeling a loop as a plasma slab with either periodic or random fine structuring. The period of trapped sausage modes is insensitive to fine structuring. For a cylinder, a similar conclusion was drawn by Chen et al. (2015a), who considered a radial density profile comprising a monolithic part and a modulation due to fine structuring in the form of concentric shells. Fine structuring, be it periodically or randomly distributed, brings changes of only a few percent to the oscillation period and damping time. The effect of finite β was found to be weak too (Inglis et al. 2009, Chen et al. 2016), as is the effect of the loop curvature (Pascoe & Nakariakov 2016). The effect of the longitudinal along the cylinder (or a loop) nonuniformity has not obtained major attention, as typically sausage oscillations are observed in short hot loops with the major radii being much shorter than the density scale height.

Density scale height: a characteristic spatial scale showing the decrease in the equilibrium density with height due to gravity

Resonant absorption: decay of collective modes in an ideal plasma by linear coupling with Alfvénic waves in which their phase speeds coincide

In a cylinder with a twisted magnetic field, i.e., in the presence of a longitudinal electric current, sausage modes are subject to resonant absorption (Giagkiozis et al. 2016). Due to this effect, the energy of MHD modes goes to the Alfvénic continuum. However, in a low-β plasma cylinder with a weak twist and an equal and constant everywhere longitudinal field B_z, the damping time associated with this mechanism is rather weak:

$$\tau_D^{(r.a.)} \approx \frac{1-\rho_e/\rho_i}{\pi^2}\left(\frac{a}{l_{rl}}\right)\left(\frac{B_z}{B_\theta}\right)^2 \frac{L}{C_{A_i}}, \qquad 2.$$

where $l_{rl} \ll a$ is the width of the resonant layer determined by the steepness of the radial profile of the density, and $B_\theta \ll B_z$ is the azimuthal field at the resonant layer. The sausage mode described by Equation 2 is in the trapped regime.

2.2. Kink Modes

Kink modes are nonaxisymmetric, $m = 1$, perturbations of the plasma cylinder, resembling transverse oscillations of a string. In the long wavelength limit, these modes become weakly compressible and are then sometimes referred to as Alfvénic (e.g., Goossens et al. 2012). Kink modes are trapped for all $k_\parallel$, and their phase speed is between C_K in the long-wavelength limit and C_{A_i} for large $k_\parallel$. Like any transverse waves, kink modes could be linearly or circularly polarized. Kink modes can be accompanied by perturbations of the optically thin emission intensity, produced by the oscillation of the apparent column depth of an observed segment in the oscillating loop (e.g., Yuan & Van Doorsselaere 2016).

In the case of smoothly varying radial profiles of the equilibrium plasma quantities, the radial structure of the perturbations is described by a solution of an eigenvalue problem constituted by a single second-order ordinary differential equation (ODE), with respect to the radial coordinate, and the boundary conditions at the axis and infinity. However, the coefficient in front of the term with the highest derivative can become zero if the phase speed of the perturbation is equal to the Alfvén or tube speeds at a certain radius. In other words, the ODE would have two singularities, known as Alfvénic and cusp singularities. Kink modes are effectively coupled to the Alfvénic continuum in the vicinity of the resonant layer; i.e., they experience resonant absorption (see, e.g., Goossens et al. 2011 for a comprehensive review). The damping profile for a resonantly damped kink oscillation excited by a nonresonant driver can be approximated as $A(t)\cos(2\pi t/P_{kink})$, where

$P_{\rm kink}$ is the period, and the amplitude varies in time as

Kelvin–Helmholtz instability (KHI): occurs in shear flows and is characterized by growing transverse perturbations and formation of so-called KHI vortices or rolls

$$A(t) = \begin{cases} A_0 \exp\left(-\dfrac{t^2}{2\tau_{\rm G}^2}\right) & t \le t_{\rm s} \\ A_{\rm s} \exp\left(-\dfrac{t - t_{\rm s}}{\tau_{\rm exp}}\right) & t > t_{\rm s} \end{cases}. \quad 3.$$

Here $\tau_{\rm G} = 2P_{\rm kink}/(\pi\mathcal{R}\epsilon^{1/2})$ and $\tau_{\rm exp} = 4P_{\rm kink}/(\pi^2\mathcal{R}\epsilon)$ are the characteristic times of the Gaussian and exponential damping regimes, determined by the parameters $\mathcal{R} = (\rho_{\rm in} - \rho_{\rm ex})/(\rho_{\rm in} + \rho_{\rm ex})$; the regime switching time $t_{\rm s} = \tau_{\rm G}^2/\tau_{\rm exp}$; and $A_{\rm s} = A(t = t_{\rm s})$ (e.g., Hood et al. 2013, Pascoe et al. 2013a). The parameter ϵ is determined by the steepness of the radial density profile near the resonant layer, $\epsilon = l_{\rm rl}/a$. The duration of the initial, Gaussian phase of the damping increases with the decrease in the density contrast in the cylinder, i.e., when $\rho_{\rm ex} \to \rho_{\rm in}$.

The sharp radial gradient of the shear flows generated by the wave in the vicinity of the resonant layer may lead to the onset of Kelvin–Helmholtz instability (KHI). When the azimuthal component of the perturbed velocity exceeds a certain threshold value, the resonant shell gets destabilized. As the main velocity component is the azimuthal one, i.e., perpendicular to the magnetic field, the field cannot provide the stabilizing effect. The generation of KHI vortices in numerical simulations of a resonantly absorbed kink mode was first demonstrated by Terradas et al. (2008a). The symmetry of the problem in the azimuthal direction allows one to consider KHI perturbations of the resonant layer as higher m harmonics. If the resonant (shear flow) layer is infinitely thin, and the equilibrium plasma density and magnetic field are the same on either side of the resonant layer, the condition for the onset of KHI could be estimated as

$$v_\phi > C_{\rm A}^{\rm (rl)} k_\parallel a/m, \quad 4.$$

where $C_{\rm A}^{\rm (rl)}$ is the Alfvén speed at the resonant layer. As the parallel wavelength of the kink oscillations observed in the corona is about two orders of magnitude greater than typical minor radii of the loops, a, the product $k_\parallel a$ is very small. Thus, KHI can occur for rather low amplitudes of the shear flows. A more rigorous estimation should account for the finite width of the resonant layer, including its broadening caused by the finite numerical resolution. Also, the azimuthal component of the magnetic field associated with the shear flows in the wave could provide a stabilizing effect. According to Terradas et al. (2008a), the first unstable azimuthal mode corresponds to $m = 5$, and its growth time is shorter than the kink oscillation period. Another reason for the onset of the nonlinear, amplitude-dependent effect in an apparently low-amplitude kink wave is that, despite the ratio of the azimuthal velocity in the wave to the local Alfvén speed being very low, the displacement amplitude of the oscillations is observed to be several times greater than the minor radius of the loop. The KHI of the resonant layer could enhance plasma heating by producing additional small spatial scales and spreading the heated volume in the radial direction (e.g., Karampelas & Van Doorsselaere 2018). A number of follow-up numerical studies confirmed the KHI effect on the enhanced damping of kink oscillations. In particular, Antolin et al. (2017) demonstrated that the development of KHI in an oscillating loop with an initial radial gradient of the temperature leads to an out-of-phase intensity and Doppler velocity modulation of coronal emission spectral lines. Howson et al. (2017) addressed the suppression of KHI by finite, possibly anomalous viscosity and resistivity.

Additional damping could be caused by the oscillation tunneling. This effect occurs if properties of the external medium, in particular, the local fast speed, change at a certain sufficiently small distance from the oscillating loop. In the nearest vicinity outside the oscillating loop, determined by Equation 1, the perturbation is evanescent; i.e., the loop acts as a cavity for the fast

wave. But if, because of the nonuniformity of the external medium, at some distance from the loop the perturbation becomes oscillatory again, there will be energy leakage in the radial direction. In particular, this effect could be important for vertically polarized kink oscillations in a coronal loop surrounded by a stratified atmosphere (e.g., Van Doorsselaere et al. 2009). For horizontally polarized kink oscillations, the tunneling effect may lead to the excitation of the oscillations in remote plasma nonuniformity (e.g., Soler & Luna 2015, and references therein). The effect of the loop curvature on kink oscillations, including wave tunneling, was discussed in detail in terms of a semitoroidal loop model by Van Doorsselaere et al. (2009). In particular, the oscillations polarized in the plane of the curved loop and across it, e.g., vertically and horizontally polarized kink oscillations of a loop situated in a vertical plane, are found to have only slightly different properties, less than 1%, that are not observationally noticeable. Likewise, the effect of the curvature on the damping time is less than 10%.

The waveguiding magnetized plasma structure may have a multistranded internal structure. Such a complex plasma structure still can show a coherent collective oscillatory behavior, resembling an oscillation of a rope consisting of a number of individual threads. The kink oscillation period has been numerically demonstrated to be about that of an equivalent homogeneous loop with the same mass and magnetic field strength (Terradas et al. 2008b). Thus, the internal fine structuring does not change the global oscillatory behavior much. Another important finding is that the existence of regular magnetic surfaces, such as cylindrical shells, are not necessary for the efficient resonant absorption damping, demonstrating that resonant absorption is a robust damping mechanism. A similar conclusion was drawn by Pascoe et al. (2011), who numerically modeled a kink wave propagating along a cylinder with a random radial density profile. In follow-up work, De Moortel & Pascoe (2012) performed numerical simulations of a kink wave guided by a bundle of 10 closely packed plasma cylinders, with random positions and density contrasts. Distances between the neighboring cylinders did not exceed their radii. The wave was excited by a harmonic transverse displacement of the bundle. The displacement lasted during one period of the sinusoid. The experiment showed the generation of a propagating wave with the mean period ~2/3 of the exciting sinusoid. In contrast, Luna et al. (2010) considered oscillations of a multistranded loop in terms of the T-matrix formalism and concluded that the oscillatory behavior of such a system cannot be properly described by an equivalent monolithic loop. However, it is natural to expect that the decrease in the average distance between the individual strands should enhance their coupling, restoring the collective behavior.

Major attention has been paid to the effect of the longitudinal nonuniformity on the kink mode. In particular, it is motivated by the use of standing kink oscillations for coronal seismology (see Section 8.1). The ratio of the fundamental and second-harmonic periods carries information about the variation of the kink speed and, hence, the density and/or magnetic field along the loop (Andries et al. 2009). Making different assumptions about the longitudinal profiles of the equilibrium quantities, different authors obtained different formulae connecting ratios of periods of different harmonics with parameters of the longitudinal nonuniformity. For long-wavelength kink oscillations, i.e., considering that the parallel wavelength is much greater than the minor radius of the loop, the effect of the variation of the equilibrium parameters along the loop could be taken into account using the formalism developed by Dymova & Ruderman (2005). Neglecting the magnetic twist, the longitudinal structure of the kink oscillation is given by the equation

$$\frac{\mathrm{d}^2(B_{z0}V_r)}{\mathrm{d}\,z^2} + \frac{1}{2R}\left(\frac{B_{r0}}{B_{z0}} + 4\frac{\mathrm{d}R}{\mathrm{d}z}\right)\frac{\mathrm{d}(B_{z0}V_r)}{\mathrm{d}z} + \left[\frac{\omega^2}{C_K^2} + \frac{1}{2R}\frac{\mathrm{d}(B_{r0}/B_{z0})}{\mathrm{d}z} + \left(\frac{\mathrm{d}R/\mathrm{d}z}{R}\right)^2 + \frac{\mathrm{d}^2R/\mathrm{d}z^2}{R}\right]B_{z0}V_r = 0, \qquad 5.$$

INFINITE MAGNETIC FIELD APPROXIMATION

Infinite magnetic field approximation is the approximation in which slow waves are considered to propagate at the sound speed, strictly along the magnetic field, which acts only as an infinitely stiff guiding background. The perturbations of the field are neglected, and the wave properties are independent of it. The governing equations are the set of acoustic equations for plane waves.

where $R(z)$ is the variation of the equilibrium minor radius along the loop; linked with the variation of the parallel and radial components of the magnetic field, $B_{z0}(z)$ and $B_{r0}(z)$, the quantities of B_{z0} and V_r are taken at the loop's axis while B_{r0} is at its boundary, and $C_K(z)$ is the local kink speed (Verth & Erdélyi 2008). Equation 5 should be supplemented by boundary conditions at footpoints, i.e., $V_r(z = 0, L)$, constituting an eigenvalue problem. Different eigenvalues and corresponding eigen functions describe oscillation periods and parallel structures, respectively, of different parallel harmonics, and their ratios.

2.3. Slow Modes

Slow, or longitudinal, modes are characterized by predominantly parallel flows along the loop, and $C_T < V_{ph} < C_s$. Properties of slow modes with different m do not differ much from each other and, hence, are not considered separately. Typically, the modeling of slow modes in a low-β plasma is made in the infinite magnetic field approximation (see the sidebar titled Infinite Magnetic Field Approximation), in which the waves propagate at the sound speed. Such a simplification can be validated by the following estimation: For a plasma $\beta < 0.1$, the sound speed differs from the tube speed by less than 4%. In this limit, weakly nonlinear propagating slow modes are described by the equation

$$\frac{\partial u}{\partial z} - \alpha_D \frac{\partial^2 u}{\partial \xi^2} + \alpha_{NL} u \frac{\partial u}{\partial \xi} = 0, \qquad 6.$$

where z is the field-aligned coordinate, $\xi = z - C_s t$, and the coefficients are $\alpha_{NL} = (\gamma + 1)/2C_s$ and $\alpha_D = 2\eta/3\rho_0 C_s$, with the viscosity coefficient η (e.g., Afanasyev & Nakariakov 2015). Other dissipative processes, e.g., thermal conduction, could be included in α_D. In particular, Equation 6 describes a quadratic dependence of the damping time upon oscillation period. The nonlinear term describes the wave steepening due to the parallel nonlinear cascade. The inclusion of the nonlinear term is motivated by weak dispersion of slow modes, which may not suppress even weakly nonlinear effects in those waves.

Slow modes of a plasma cylinder are locally oblique, as their effective radial wave number determined by the cylinder's radius is usually much bigger than $k_\parallel$. For higher values of plasma β, the local obliquity of slow modes with small $k_\parallel$ becomes important, making the magnetic effects on the wave dynamics nonnegligible. In this regime, the speed of slow waves approaches the tube speed C_T at $k_\parallel \to 0$. This effect is properly accounted for by the thin flux tube approximation. Its generalized version allows for the consideration of effects of geometrical dispersion, caused by a finite ratio of the parallel wavelength and the cylinder's radius, and also of the magnetic twist and cylinder's rotation (Zhugzhda 1996). In this approximation, the evolutionary equation for long-wavelength slow waves in an untwisted, nonrotating, plasma cylinder has the same functional form as Equation 6, whereas the coefficients α_{NL} and α_D acquire additional dependence on the magnetic

field,

$$\alpha_{\rm NL} = \frac{C_{\rm T}}{2(C_{\rm s}^2 + C_{\rm A}^2)}\left[3 + (\gamma+1)\frac{C_{\rm A}^2}{C_{\rm s}^2}\right],\ \alpha_{\rm D} = \frac{(\gamma-1)^2\kappa T_0 C_{\rm T}}{2\rho_0 C_{\rm s}^4} + \frac{\eta}{6\rho_0 C_{\rm T}}\left(3 + \frac{C_{\rm A}^2}{C_{\rm s}^2 + C_{\rm A}^2}\right), \quad 7.$$

where the effect of the field-aligned thermal conductivity κ is included in the damping (Afanasyev & Nakariakov 2015). Finite β effects decrease the coefficient $\alpha_{\rm NL}$; i.e., they suppress the nonlinear cascade.

Conventionally, the damping of slow modes is associated with the field-aligned thermal conductivity effect (see, e.g., Ofman & Wang 2002, De Moortel & Hood 2003, Owen et al. 2009). It is considered to be sufficient for the interpretation of observed properties of slow waves both qualitatively and quantitatively in certain physical conditions, i.e., for a specific combination of the equilibrium plasma density and temperature. In other physical conditions, though, it was shown to be less successful (e.g., De Moortel 2009). A parameter controlling the efficiency of the thermal conduction is the conduction time $\tau_{\rm cond} = \rho_0 C_V L_\parallel^2/\kappa$, where the parallel conductivity coefficient in the Spitzer form is $\kappa = 10^{-11} T_0^{5/2}\ {\rm W\,m^{-1}\,K^{-1}}$, and $C_V = (\gamma - 1)^{-1} k_{\rm B}/m_{\rm p}$ is the specific heat capacity with $k_{\rm B}$ being the Boltzmann constant and $m_{\rm p}$ the proton mass. The time $\tau_{\rm cond}$ is highly sensitive to the equilibrium plasma temperature, T_0, density, ρ_0, and the characteristic spatial scale, $L_\parallel$. The dependence of $\tau_{\rm cond}$ on the temperature is shown in **Figure 1*a*** for various wavelengths. For illustration, consider a fundamental standing slow mode with the wavelength determined as double the loop length $L = 116$ Mm. The thermal conduction time is sufficiently longer than

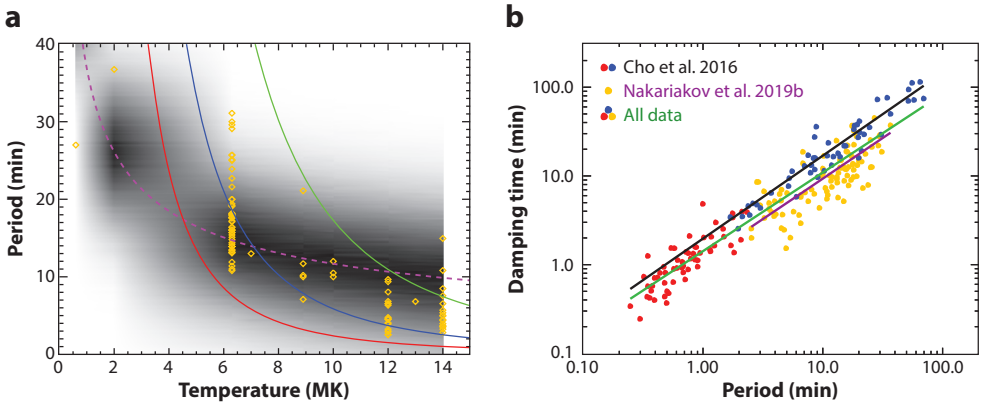

Figure 1

Statistical properties of slow oscillations observed in the solar and stellar coronae. (*a*) Oscillation periods, $P_{\rm slow}$ (*yellow diamonds*), against the temperature of the oscillating loop, T, for the events available in the literature (see Nakariakov et al. 2019b). The magenta dashed line shows the best fit of the model $P_{\rm slow} \propto T^{-1/2}$ into the observed data cloud. The background black and white shading shows the posterior predictive probability distribution obtained with MCMC, which highlights areas in which data points could be observed according to the model. The red, blue, and green lines show the estimation of the thermal conduction time for the plasma concentration of 10^9 cm^{-3} and loop lengths of 74 Mm (*red*), 116 Mm (*blue*), and 199 Mm (*green*). (*b*) Dependence of the damping time upon the oscillation period, for solar (*red circles*) and stellar (*blue circles*) QPP of the SUMER class (Cho et al. 2016) and for SUMER oscillations (Nakariakov et al. 2019b, *yellow circles*). The straight lines show best fits of the corresponding data clouds: the SUMER data set (*purple line*); the whole QPP data set (*black line*), and the entire data set (*green line*) by the power-law functions (see Sections 6.1 and 6.3 for details). The fitting and the estimation of uncertainties in both panels were performed with the MCMC technique. Abbreviations: MCMC, Markov chain Monte Carlo; QPP, quasi-periodic pulsation; SUMER, Solar Ultraviolet Measurements of Emitted Radiation spectrometer.

typical slow oscillation periods in the range of temperatures from ∼1 to 5 MK (from a few to a few tens of minutes), which makes the effect of the thermal conduction on the slow wave weak in this temperature range. In a hotter plasma, from ∼5 to 12 MK, $\tau_{\rm cond}$ is roughly comparable with the slow oscillation period, indicating high efficiency of the wave damping by thermal conduction. For temperatures above 12 MK, $\tau_{\rm cond}$ becomes substantially shorter than the slow oscillation period, implying that the thermal conduction rapidly smooths out any temperature gradient along the field and thus making the slow wave nearly isothermal. In the lower thermal conduction limit, the conductive damping time of slow waves, $\tau_{\rm D}^{\rm cond} = 2C_{\rm V}\rho_0\gamma(\gamma-1)^{-1}\kappa^{-1}k_{\parallel}^{-2}$, decreases with temperature down to some value, after which the wave dynamics approaches the isothermal regime and therefore becomes independent of the thermal conductivity (e.g., Porter et al. 1994, Krishna Prasad et al. 2019). The existence of the isothermal regime indicates the importance of additional dissipative mechanisms for slow modes in the corona. It could be viscous damping (Owen et al. 2009, Wang et al. 2018), longitudinal nonuniformity (De Moortel & Hood 2004, Konkol et al. 2010), nonlinear damping (e.g., Verwichte et al. 2008, Ruderman 2013), mode coupling (De Moortel et al. 2004), or damping by the misbalance between coronal heating and radiative cooling processes (Nakariakov et al. 2017, Kolotkov et al. 2019). A relative efficiency of these damping mechanisms in specific coronal conditions needs to be revealed.

Identification of an appropriate damping scenario has implications for seismological diagnostics of the coronal plasma by slow waves (Section 8.4). For example, one of the unresolved puzzles is the observationally obtained linear scaling of the damping time with the oscillation period (see Section 6.1), whereas the damping of linear slow waves by both thermal conduction and viscosity suggests a quadratic dependence, as readily follows from Equations 6 and 7 (see also Banerjee & Krishna Prasad 2016, their table 1). Various damping scenarios were assessed by Wang et al. (2018), aimed at revealing the reason for this unexpected linear scaling. Numerical simulations were performed within a 1D hydrodynamic nonlinear model, with a flow pulse driven near one footpoint, taking into account possible, seismologically motivated, suppression and enhancement of the thermal conduction and viscosity coefficients by a factor of 3 and 15, respectively. An interesting future avenue is offered by Bradshaw et al. (2019), who explored scaling laws between global parameters of a loop for various forms of the field-aligned thermal conduction. In addition to the collision-dominated Spitzer heat flux $\kappa \propto T^{5/2}$, the turbulence, $\kappa \propto T^{-1/2}$, and free-streaming, $\kappa \propto T^{3/2}$, forms of the heat flux were considered. It was established that the Spitzer heat flux dominates over the other heat fluxes in both flaring (i.e., more turbulent) and quiet Sun conditions for a sufficiently dense ($10^{10.5}$ cm^{-3}) and relatively warm ($10^{6.2}$ K) plasma. However, for a less dense (10^9 cm^{-3}) and hotter ($10^{7.5}$ K) plasma, the turbulence-dominated and free-streaming heat fluxes were found to be more efficient in active and quiet Sun regions, respectively. The additional mechanisms for thermal conduction could have important impacts on the slow wave dynamics and need to be taken into account in the modeling.

Another large segment of the ongoing activity in theoretical modeling of slow modes is devoted to the problem of the wave excitation. For example, within a 1D infinite magnetic field radiative model including the effect of gravitational stratification, heat conduction, bulk viscosity, and external heat input, Tsiklauri et al. (2004) showed that the second spatial harmonic of the slow wave can be effectively excited by an impulsive energy release situated near the apex of the loop. Using a similar 1D dissipative model, Selwa et al. (2005) demonstrated dependence of the fundamental and second harmonic generation on the location of the impulsive trigger. More specifically, pulses situated closer to the loop footpoint were shown to excite the fundamental mode, whereas those located closer to the loop apex result in the excitation of the second harmonic. Likewise, pulses situated in between the loop footpoint and the apex can simultaneously excite a number of spatial harmonics, among which two lowest-frequency modes give the greatest contribution. Similar

results were obtained analytically by Taroyan et al. (2005). Ogrodowczyk et al. (2009) generalized these findings by taking into account the effect of a 2D curved magnetic field that allowed for a more effective excitation of standing slow waves. In addition, the slow wave leakage into both the photosphere-like layer and the ambient coronal medium was detected. Full-scale 3D radiative MHD simulations of the slow wave excitation in fan-like loops were performed in a series of works by Ofman et al. (2012), Wang et al. (2013), and Provornikova et al. (2018) that address the question of whether the observed EUV intensity disturbances propagating at about the local sound speed are waves or quasi-periodic flows. Impulsive injections of a hot plasma at the loop footpoint were confidently shown to develop into a slow wave propagating upward along the loop. Efficient excitation of slow waves in impulsively heated coronal loops and their manifestation in the X-ray flare emission were demonstrated by Reale (2016) and Reale et al. (2018) in terms of a nonlinear 1D hydrodynamic model, accounting for the process of the loop formation by evaporation of a chromospheric material and evolution of the loop parameters with time. In other words, the plasma transport coefficients[6] in these simulations were allowed to vary with time, thus making different physical processes dominate in the wave dynamics at different stages of the loop evolution.

An intrinsic property of the solar corona, potentially influencing the dynamics of slow modes, is its thermodynamic activity, which maintains a delicate balance between energy losses via optically thin radiation and thermal conduction and some unidentified heating process operating simultaneously. Here, we do not associate the waves with the heating but consider the waves in the medium, which is somehow heated to counteract the cooling. Taking into account that the heating and cooling processes should depend differently on the plasma parameters (see, e.g., De Moortel & Browning 2015 for a recent review), the wave-induced perturbations could readily destabilize the thermal equilibrium and cause a misbalance between the plasma heating and cooling processes. In this situation, the wave can either give energy to the plasma or get energy from it. Nakariakov et al. (2017) considered the effect of the thermal misbalance on slow waves in the limit of weak nonadiabaticity, i.e., assuming the imaginary part of the oscillation frequency to be much smaller than the real part. Under this approximation, Equation 6 was generalized by adding a linear term $\alpha_{\mathrm{M}} u$. The effect of thermal misbalance is controlled by the coefficient $\alpha_{\mathrm{M}} = (\gamma - 1)[Q_\rho \rho_0 + (\gamma - 1) Q_{\mathrm{T}} T_0]/2\rho_0 C_{\mathrm{s}}^3$, where Q_ρ and Q_T are the derivatives of the combined heating/cooling function $Q(\rho, T)$ with respect to the density and temperature, respectively, evaluated at the equilibrium (see the sidebar titled Coronal Heating/Cooling Function). It was shown to either lead to an enhanced damping of slow waves, in addition to that caused by thermal conduction, or alternatively result in the wave amplification, i.e., thermal overstability. Analytical treatment of the full thermal misbalance effect on linear slow waves, without employing the assumption of weak nonadiabaticity, was developed by Zavershinskii et al. (2019) and Kolotkov et al. (2019). The thermal misbalance was shown to have two characteristic timescales τ_1 and τ_2, determined by the rates of change of the heating/cooling function with density and temperature, $\tau_1 = \gamma C_{\mathrm{V}}/[Q_T - (\rho_0/T_0) Q_\rho]$ and $\tau_2 = C_{\mathrm{V}}/Q_T$. As such, these misbalance timescales are not associated with the radiative cooling

CORONAL HEATING/COOLING FUNCTION

The coronal heating/cooling function is a combined wavelength-independent function of energy losses, by optically thin radiation, and gains, by some heating mechanism parameterized in some form, as a function of plasma parameters.

[6]Plasma transport coefficients are quantities characterizing transport processes in plasma, for example, viscosity, thermal conductivity, and electrical conductivity.

THERMAL MISBALANCE

Thermal misbalance is a wave-induced misbalance between heating and cooling rates of a thermally active plasma, leading to wave damping or amplification and to the effective wave dispersion. It can be characterized by typical rates of change of the coronal heating/cooling function with density and temperature.

time of a preheated plasma, which characterizes the cooling rate in the case of nonvarying heating (see, e.g., De Moortel & Hood 2004, Claes & Keppens 2019). Estimations show that the values of $\tau_{1,2}$ could be of the same order of magnitude as the periods of slow oscillations observed in the corona (see Sections 5 and 6.1).

Importantly, the presence of the additional characteristic times causes slow wave dispersion, manifested by the dependence of the polytropic index and phase and group speeds on the wave frequency. This misbalance-caused dispersion is not connected with the waveguide dispersion, which is rather weak for slow waves. A similar dispersion effect was discussed by Ibanez et al. (1993). A combination of the wave dispersion and amplification, both of which are caused by the thermal misbalance (see the sidebar titled Thermal Misbalance), was shown to lead to the formation of quasi-periodic slow wave trains from an initially broadband slow wave pulse, with a typical period $P_{\mathrm{TM}} \approx (\tau_1 \tau_2)^{1/2}$ that could be about several minutes or longer. In the regime of enhanced damping, the observed enhanced slow wave damping rates (see Section 5) could be readily reproduced with a reasonable choice of the heating model.

Employing the forward modeling approach, Yuan et al. (2015) simulated Doppler shift and EUV emission intensity variations by standing slow waves in flaring loops, observed by Solar Ultraviolet Measurements of Emitted Radiation (SUMER) on *SOlar and Heliospheric Observatory* (SOHO) and SDO/AIA instruments (see Section 6.1). The effects of the emission intensity asymmetry and the LoS projection were investigated for parallel slow harmonics. Fang et al. (2015) performed forward modeling of sloshing (reflecting) slow wave in a flaring loop, also manifested in the data from SOHO/SUMER and SDO/AIA. The numerical 2.5D MHD model, used for obtaining the plasma density and temperature variations, included the effects of the chromospheric evaporation. Direct comparison of the sloshing events observed by the *Hinode* X-Ray Telescope and SDO/AIA in hot coronal loops with the results of a 2.5D MHD simulation and subsequent synthesizing of AIA 94-Å images was performed by Mandal et al. (2016b). The simulated results suggested that the observed sloshing wave could be excited by a footpoint heating source. Mandal et al. (2016a) performed forward modeling of frequency-dependent damping of propagating slow waves (see Section 5) in a 3D coronal loop model. The results obtained for four oscillation periods showed an almost linear dependence of the damping length on the period, for which the field-aligned thermal conduction was invoked as a possible damping mechanism. However, this estimation would benefit from taking more data points, i.e., different wave periods, into account.

3. SAUSAGE OSCILLATIONS OF CORONAL LOOPS

Since the interpretation of 16-s and 9.5-s periodic variations of the microwave emission from a spatially resolved flaring loop as sausage oscillations (Melnikov et al. 2005), observational detections of the sausage mode have remained rather sporadic. This is owing to the insufficient time resolution of EUV telescopes and intrinsically poor spatial resolution of radio instruments. But, the main difficulty is the inherent suppression of the observed modulation of the optically thin

emission intensity by the plasma density and magnetic field perturbations in the sausage wave (e.g., Gruszecki et al. 2012). In the optically thin regime, thermal emission is proportional to the density squared,

$$\mathcal{I}(t) \propto \iint_{(\text{pixel})} \mathrm{d}A \int_{(\text{LoS})} \rho^2(t)\mathrm{d}s, \qquad 8.$$

where the outer integration is over the pixel size in the plane of the sky, and the internal integration is along the LoS. In the sausage mode the flows redistribute the plasma in the radial direction. Hence, if the pixel size is comparable with or bigger than the oscillating plasma structure, e.g., a coronal loop, the same plasma remains inside the same pixel and along the LoS during all phases of the oscillation, and the observed emission intensity modulation by the sausage wave could be orders of magnitude lower than the wave amplitude. This problem could be partially mitigated if the LoS is not perpendicular to the cylinder representing a segment of the oscillating loop (Antolin & Van Doorsselaere 2013). The sausage mode can also be seen in the spectral data as the emission line broadening. A similar effect takes place in the modulation of the gyrosynchrotron emission too, and additional information could be obtained by comparing parameters of the oscillation at different parts of the gyrosynchrotron spectrum (Kuznetsov et al. 2015).

In the lack of a systematic statistical study of sausage oscillations and their possible candidates, we illustrate the observational detections of sausage oscillations by a few case studies. Tian et al. (2016) interpreted 25-s oscillations of the intensity and Doppler shift of the Fexxi in a flare as a fundamental harmonic of the sausage oscillation. This conclusion was supported by the observed quarter-period phase shift between the Doppler shift and intensity oscillations. Mészárosová et al. (2016) found signatures of sausage oscillations with the characteristic periods of 0.7 s and 2 s in the broadband microwave emission around 1 GHz. Carley et al. (2019) interpreted 2.3-s pulsations of a radio emission source observed during a flare as the modulation of electron acceleration efficiency by a loss-cone instability associated with a sausage oscillation.

There are several interpretations of quasi-periodic pulsations (QPPs; see the sidebar titled Quasi-Periodic Pulsations) detected in spatially unresolved observations of solar flares, in terms of the sausage mode. In particular, short-period (1–40 s) QPPs of the electromagnetic emission produced by flares are often associated with sausage oscillations (e.g., Van Doorsselaere et al. 2016; see also Section 6.3). For example, 8.5-s QPPs in the flaring emission of the chromospheric and coronal origin were interpreted as a sausage oscillation (Van Doorsselaere et al. 2011a). Yu et al. (2013) interpreted 1-s wiggles of the individual lanes in a zebra pattern observed in the dynamic microwave spectrum of a type IV radio burst as the modulation of the electron plasma density and magnetic field by a sausage oscillation. Drifting quasi-periodic modulation of zebra-pattern lanes in the dynamic radio spectrum of another type IV radio burst was linked with a sausage wave propagating upward at the speed of several million meters per second by Kaneda et al. (2018).

QUASI-PERIODIC PULSATIONS

QPPs are oscillatory modulations of solar and stellar flaring light curves. The term "quasi" reflects the nonstationary and nonharmonic nature of the repetitive pulsations, usually manifested in observations. Often, QPPs show several cycles of the oscillation only, and pronounced modulations of the amplitude and period. Usually, QPPs appear in a certain phase of the flare.

4. KINK OSCILLATIONS OF CORONAL LOOPS

Kink oscillations of coronal loops were discovered as periodic, rapidly decaying transverse displacements induced by an energy release nearby, detected in the EUV band at 171 Å and 195 Å (see, e.g., Nakariakov et al. 2016b and Wang 2016 for recent reviews), and have become one of the most studied wave phenomena in the corona. The displacement oscillations usually have a clear antinode at the loop apex and nodes at the footpoints. All segments of the loop usually oscillate in phase, indicating that the oscillation is the fundamental parallel harmonic of the kink mode of the loop. Higher parallel harmonics have been detected too, though less often. Typical periods of kink oscillations are of several minutes and typical displacements are of several million meters, which allows the oscillations to be well resolved with modern EUV imagers. The impulsively excited oscillations damp rapidly, typically in fewer than 6 cycles. More specifically, observed kink oscillation periods span from 1 min to 29 min, and the apparent displacement amplitudes are 1–10 Mm, which is typically ~1% of the loop length (Nechaeva et al. 2019). Propagating kink waves guided by field-aligned plasma nonuniformities have been identified in the imaging observations of the Doppler shift (e.g., Tomczyk & McIntosh 2009, Morton et al. 2016). The waves propagate outward from the bottom of the corona, along the apparent direction of the magnetic field and rapidly damp with height. The waves have projected amplitudes of about 1 km $s^{-1}$and periods in the vicinity of 5 min.

In imaging data, kink oscillations are usually detected by eye, by watching a movie showing the behavior of a certain active region. The standard data analysis technique for a more rigorous analysis is the time–distance method. In a data cube, which consists of a pile of images of the oscillating loop taken at different instants of time, a slit is selected in the direction of the displacement, i.e., perpendicular to an oscillating segment of the loop (**Figure 2*a***). The width of the slit is usually a few million meters; i.e., the signal is summed up along a segment of the loop in each EUV image. Along the slit, one sees the variation of the EUV emission intensity with a local maximum corresponding to the loop's location. As the loop oscillates transversely, the location of maximum intensity along the slit changes from frame to frame. Stacking the slits made in consecutive images, one gets a time–distance plot (or map) which visualizes the transverse movements of the loop (**Figure 2*b***). The oscillatory pattern in the time–distance map can then be best-fitted by some guessed analytical function, for example, by a harmonic function with an exponential or Gaussian damping, or their combination. Parameters of the best-fitted function give us the oscillation period and initial phase, the apparent displacement amplitude, and the characteristics of the damping.

The search for kink oscillation events in solar cycle 24 has resulted in the detection and analysis of 223 kink oscillation events (Nechaeva et al. 2019). This number is sufficiently large to obtain statistical properties of observed oscillations and use them for the validation of theoretical models (see Section 2.2). **Figure 3*a*** shows the empirical scaling of the oscillation period P_{kink} with the loop length L. The obvious linear increase in the period with the length supports strongly the interpretation of kink oscillations as natural oscillations of loops, i.e., the fundamental kink mode with $m = 1$, $n_L = 1$, and $n_R = 0$. Taking the parallel wavelength as $2L$, we estimate the average kink speed as $C_{\mathrm{kink}} = 1328 \pm 53$ km s^{-1}. The width of the data cloud, apart from usual errors in the measurements, could be attributed to different kink speeds in different loops. In addition, for longer loops, one should take into account the nonuniformity of the kink speed along the loop caused by the density stratification and, possibly, the increase in the minor radius with height.

It is instructive to estimate the kinetic energy associated with a typical kink oscillation. For a period of 300 s and initial displacement of 5 Mm, we estimate the speed of the displacement as ~70 km s^{-1}. The mass of the oscillating loop could be estimated by the product of the proton mass, the electron concentration, say, 4×10^9 cm^{-3}, and the loop's volume. The mass of a loop of

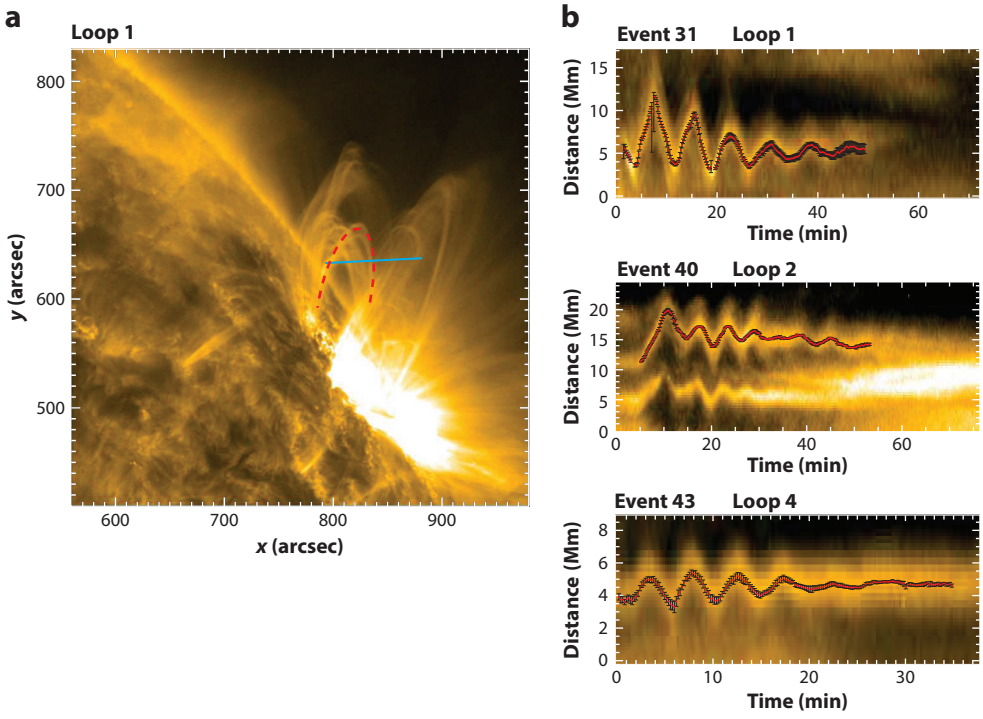

Figure 2

(*a*) An active region in the solar corona observed at 171 Å with the *Atmospheric Imaging Assembly* on the *Solar Dynamics Observatory* with a pronounced set of bright plasma loops. The oscillating loop is shown by a dashed red curve. The blue line shows the slit used to create a time–distance map. (*b*) Typical time–distance maps with examples of kink oscillations. The red symbols with the black error bars show the oscillatory patterns. Panel *a* adapted from Pascoe et al. (2016a), and panel *b* from Pascoe et al. (2016b).

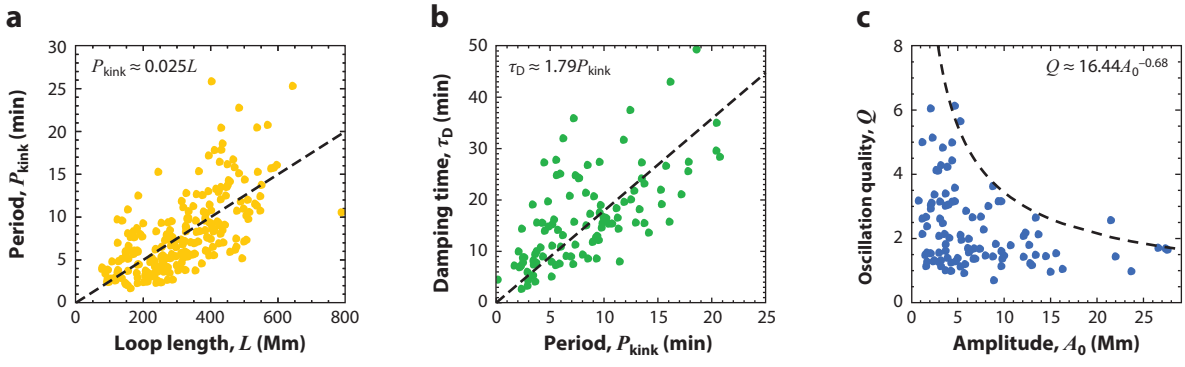

Figure 3

Relationships between different parameters of decaying kink oscillations of coronal loops, observed during solar cycle 24. (*a*) The oscillation period versus the loop length. (*b*) The exponential damping time versus the oscillation period. (*c*) The oscillation q-factor versus the projected displacement amplitude. The dashed curves show the best-fitting curves. Adapted from Nechaeva et al. (2019).

the minor radius of 1 Mm and length of 200 Mm is $\sim 4 \times 10^{12}$ g. Thus, the kinetic energy of a typical kink oscillation is $\sim 10^{26}$ erg, which is lower than that in the smallest detected solar flare. Thus, the detected decaying kink oscillations occur too rarely and are too weak to contribute to heating of the coronal plasma.

4.1. Excitation of Kink Oscillations

There are several alternative mechanisms proposed for the excitation of kink oscillations. The mechanisms could be grouped in three categories that have a clear analogy with the excitation of oscillations in a pendulum. The pendulum oscillations can be excited by a sudden kicking of the load when it is in the equilibrium, a sudden release of the load slowly displaced from the equilibrium, or a gradual excitation of the oscillation by some direct or parametric resonant force. The former two cases could be considered as a sudden deposition, in comparison with the oscillation period, of kinetic or potential energy, respectively, to the pendulum representing the loop.

In the early days, kink oscillations were believed to be induced by a high-amplitude fast magnetoacoustic wave, perhaps a fast shock, excited by a nearby flare. A freely propagating fast wave is locally longitudinal; i.e., the induced flows of the plasma are in the direction of the wave propagation. Such a blast wave could indeed cause the initial displacement of the loops surrounding the flaring site (see, e.g., Ofman 2007, and Terradas 2009 for a review). But, this mechanism has difficulties with the explanation of the large, up to several minor radii of the loop, initial displacement. Also, it does not explain the selectivity of the excitation, i.e., why only certain loops get displaced by the blast wave. Another possibility is the initial displacement of a loop by some sudden evolution of the active region, for example, an expansion or contraction (e.g., an implosion) of a loop system caused by some major perturbation of the total magnetic pressure, localized nearby (see, e.g., Gosain 2012 and Simões et al. 2013 for observational examples). In particular, such a sudden perturbation of a loop system can be produced by a sudden removal of magnetic energy from the corona by a filament eruption or reconnection leading to a flare. For example, in the scenario proposed by Russell et al. (2015), the equilibrium achieved by the magnetic tension force directed from the loop downward and the total pressure gradient force applied at the loop from the magnetic field under the loop are perturbed by a sudden decrease of coronal magnetic energy, and consequently magnetic pressure, caused by a flare under the loop. As the loop's magnetic field is not involved in the flare, the force imbalance pushes the loop downward to a new equilibrium. Because of the inertia the loop overshoots the new equilibrium and oscillates around it in the kink mode.

Antolin et al. (2018) suggested that kink oscillations could be excited by a collision of unsteady counter-streaming upflows along the loop, which are generated at the footpoints. Kink oscillations are excited if the fronts of the colliding flows are not exactly parallel to each other. Oscillations with the observed amplitudes were successfully reproduced in a numerical experiment for the plasma β between 0.09 and 0.36. Kink oscillations, polarized in the plane of the loop, could be excited by an upflow pulse at one or both footpoints, by the centrifugal force connected with the loop's curvature (Zaitsev & Stepanov 1989). During the upflow, the force displaces the loop from the equilibrium, making it expand. Numerical simulations have shown that a sine-like pulse with the amplitude of 80 km s^{-1} could excite the fundamental kink mode of a 1-Mm displacement amplitude in a loop with the major radius of 90 Mm and the density contrast of 10 (Kohutova & Verwichte 2018).

All the mechanisms described above could be attributed to the first group, in which the oscillation is excited kinetically from the equilibrium position, by a sudden transfer of kinetic energy to the loop. Concerning the second group, it is believed that kink oscillations could build up in response to the periodic or random transverse shuffling of the footpoints, caused by photospheric

motions, e.g., the granulation simulated by a monochromatic or random footpoint movements (e.g., De Moortel & Pascoe 2012, Antolin et al. 2016). Hindman & Jain (2008) considered the buffeting excitation of kink oscillations by photospheric motions associated with p-modes. It was shown that the excited periods are in the vicinity of 5 min. In addition, kink oscillations could be gradually built up as a response of the loop to a centrifugal force associated with periodic slow waves propagating upward from the footpoint(s) (see Section 5). However, these scenarios are not consistent with the observed almost instantaneous increase in the oscillation amplitude.

A statistical approach has revealed that the most probable mechanism for the excitation of decaying kink oscillations is by initial mechanical displacements of loop (Zimovets & Nakariakov 2015), i.e., by displacing and releasing the load of the pendulum. The ratio of the distance between the energy release site and the oscillating loop, and the delay time between the energy release and the beginning of the oscillation, gives us the characteristic speed of the agent that performs the excitation. In ∼80% this speed was found to be lower than 500 km s^{-1}, i.e., about two times lower than the fast wave speed expected in coronal active regions. Furthermore, only 40% of the kink oscillation events are accompanied by type II radio bursts, which are associated with coronal blast waves. By contrast, it was observationally established that in 95% of observed events, kink oscillations are excited by the initial displacement of the loops by a slowly moving (e.g., erupting and/or expanding) plasma structure, such as an unstable flux rope. Thus, only the loops that are mechanically displaced from the equilibrium by the eruption become oscillating. However, this "potential excitation" mechanism has not received proper theoretical attention yet, despite the obvious indication of its dominance. In particular, the partition of the energy between different parallel harmonics remains unknown.

4.2. Damping of Kink Oscillations

The scaling of the damping time with the oscillation period (**Figure 3*b***) seems to support the linear dependence of the damping time on period, established for the resonant absorption mechanism (see Equation 3 and the discussion in Ofman & Aschwanden 2002). The broad scattering of the data points in that plot could be attributed to the intrinsic difficulties in the estimation of the damping time of the low-quality oscillations, the scattering of the density contrast ratio ρ_i/ρ_e, or different radial density profiles in the sampled loops. In addition, the dependence of the decaying kink oscillation q-factor on the amplitude (**Figure 3*c***) indicates that the oscillation damping is a nonlinear process. The q-factor scales with the amplitude to the power of −0.7, i.e., ∼−2/3. Possibly, the damping mechanism is KHI (see Section 2.2), which is a nonlinear effect. A decrease in the damping time with the increase in the initial amplitude, caused by KHI, has been seen in numerical simulations (Magyar & Van Doorsselaere 2016). This dependence was found to cease in plasma cylinders with the radial inhomogeneous layers thicker than 0.5 radii. But, there is a need for a dedicated study to assess whether KHI could reproduce the observationally established scaling of the q-factor with the initial amplitude. However, there is no observational evidence of a significant evolution of transverse profiles of oscillating loops during decaying kink oscillations, which would be typical of KHI. Such a measurement could be made seismologically (see Goddard et al. 2018 and Section 8.2). The main signatures of the development of KHI would be gradually widening (smoothing) boundaries of the oscillating loop, decreasing intensity, a nonvarying radius, and visible fine transverse structuring when the resolution is sufficient.

4.3. Decayless Kink Oscillations

Wang et al. (2012) discovered a new decayless regime of standing kink waves in coronal loops. Low-amplitude oscillations could be observed for several tens of oscillation cycles, with none

showing any decrease in the amplitude. In some time intervals the displacement amplitude even grows while typically remaining lower than the amplitude of decaying kink oscillations. Decayless oscillations occur in the quiet time intervals, i.e., without any association with a visible flare or eruption. Nisticò et al. (2013) demonstrated that the decaying and decayless oscillations are likely different regimes of the same standing kink mode. Low-amplitude decayless oscillations were observed before and well after a large-amplitude rapidly decaying oscillation excited by an impulsive energy release nearby (see also Allian et al. 2019). In both regimes, the oscillation periods were the same within the error bars. Anfinogentov et al. (2015) performed statistical analysis of decayless kink oscillations in 72 loops. It was established that almost every loop with a sufficiently contrasted boundary in EUV images continuously oscillates, with the apparent displacement amplitude ξ going up and down by a factor of about two at a timescale of several periods. Amplitudes span from 0.05 Mm to 0.5 Mm, with 0.17 Mm as the mean value. Oscillation period spans from 50 s to 650 s, with 251 s as the mean value. Oscillation periods show a clear linear scaling with the loop lengths, which is similar to that found for large-amplitude decaying kink oscillations. The distribution of velocity amplitudes, estimated as the ratio of the displacement amplitudes and the kink oscillation periods as $2\pi\xi/P_{\mathrm{kink}}$, does not show any pronounced, i.e., resonant, peak (Nakariakov et al. 2016a). Typical velocity amplitudes are estimated as a few kilometers per second. Duckenfield et al. (2018) detected the coexistence of fundamental and second parallel harmonics, both in the decayless regime. As expected, the longer-period, 10-min harmonic has the maximum amplitude near the loop top and oscillates in phase throughout the loop length. The shorter, 7-min harmonic is strongest further down from the apex on both legs and displays an antiphase behavior between the opposite legs.

The first spectroscopic detection of decayless kink oscillations was made by Tian et al. (2012), who found persistent, i.e., lasting for three hours, undamped oscillations in the Doppler shift of coronal emission lines with formation temperatures of ~1–2 MK in the upper part of loops. The detected oscillation periods range from 3 to 6 min. The oscillation amplitude is a few kilometers per second, which is consistent with the imaging observations of decayless kink oscillations. In addition, similar oscillatory patterns were found in the emission intensity. The intensity oscillation amplitude was ~2%. The phase shift between the Doppler shift oscillations was estimated as ~1/4 of the period.

The mechanism counteracting damping, which is intrinsic to larger-amplitude kink oscillations, e.g., caused by resonant absorption, is subject to intensive debate. Full MHD numerical simulations of an impulsively excited kink oscillation with the initial amplitude of 1% of the kink speed, combined with forward modeling of observables, suggested that the development of poorly resolved KHI vortices could extend the apparent decay time of the oscillation, which was observed in certain bandpasses (Antolin et al. 2016). However, in this scenario the oscillation eventually decays anyway. Thus, this scenario does not explain the observed behavior of decayless kink oscillations, in particular, their existence for a large number of oscillation cycles and the time intervals when the oscillation amplitude is increasing (Wang et al. 2012). The damping can be suppressed by some continuous energy supply to the oscillating loop. Guo et al. (2019) modeled a response of a plasma cylinder to a harmonic driver operating at one of the footpoints and managed to reproduce kink oscillations with a constant amplitude. However, the amplitude of oscillations of a harmonically driven oscillator with damping is highly sensitive to the difference between the frequency of the driver and the natural frequency, i.e., the effect of a resonance. In an ensemble of independent oscillators with different natural frequencies, driven by a harmonic driver, different oscillators should show different amplitudes. However, the lack of a pronounced peak in the distribution of the observed amplitudes of decayless oscillations with respect to the periods or loop lengths does not support the existence of a harmonic driver (Nakariakov et al. 2016a).

Hindman & Jain (2014) proposed that decayless kink oscillations could be reinforced by a continuously operating stochastic driver. The effect was considered in terms of a model of a two-dimensional waveguide formed by a coronal arcade.

Nakariakov et al. (2016a) described a decayless kink oscillation as a self-oscillatory process[7] caused by the effect of negative friction. In this model, the energy lost by dissipation or mode conversion is resupplied by quasi-steady external flows, e.g., supergranulation flows near the footpoints. This mechanism is analogous to producing a tune by moving a bow, i.e., the supergranulation flow, across a violin string, i.e., the loop. The amplitude is determined by the damping rate, parameters of the external flow, and the friction between the flow and the loop. Mathematically, the decayless regime corresponds to a limit cycle in the phase portrait of the ODE that models the oscillatory process. Oscillations excited with amplitudes higher than the amplitude of the limit cycle decrease to this amplitude, whereas lower-amplitude oscillations are magnified. The ability of the model to explain observational properties of decayless kink oscillations suggests the need for its further development.

5. PROPAGATING SLOW WAVES

Compressive propagating coronal slow waves are usually associated with quasi-periodic EUV and soft X-ray intensity perturbations that move upward along field-aligned plasma nonuniformities. They are observed, in particular, with the high-resolution imaging telescopes. These propagating quasi-periodic disturbances typically have small amplitudes of a few percent of the background intensity, with periods in the range of 2–10 min and propagation speeds of $\sim$70–235 km s^{-1}, which are comparable with the local sound speed. These waves are observed to decay quickly with height and with the decay length of a few tens of millions of meters. Routine observations demonstrated omnipresence of this phenomenon, occurring in both the plume and interplume regions in polar coronal holes (e.g., Gupta et al. 2010), legs of long fan-like loops in active regions (see **Figure 4** and Yuan & Nakariakov 2012), and also in plume-like structures in equatorial coronal holes and quiet Sun regions (e.g., Tian et al. 2011, Krishna Prasad et al. 2012b). These waves could be also detected spectroscopically, as Doppler shift variations and emission enhancements in the blue wing of the emission line (e.g., Verwichte et al. 2010), manifesting the in-phase behavior of the velocity and density perturbations. For comprehensive reviews of earlier observational results on the detection of propagating slow waves in coronal loops and holes, readers are referred to, e.g., De Moortel (2009) and Banerjee et al. (2011). Discussion of an alternative interpretation for the propagating EUV disturbances, in terms of quasi-periodic upflows, and its constructive criticism based on the comparison to the wave-related explanation are given by Wang (2016).

The propagation speed of quasi-periodic EUV disturbances in loops situated above sunspots and in polar coronal holes is found to depend on temperature (Kiddie et al. 2012, Gupta 2014). The estimation of the loop base temperature, inferred seismologically from the observed propagation speed and then interpreting observations as propagating slow waves, showed good agreement with the value of temperature obtained by spectroscopic diagnostic methods (Marsh & Walsh 2009). Uritsky et al. (2013) demonstrated that the speed of a propagating wave in warm fan-like structures in a non-sunspot-active region depends upon the square root of the temperature, as it should be for the sound or tube speeds. Marsh et al. (2009) took into account the projection effects in the

[7]Self-oscillation (or self-sustained oscillation) is the generation and maintenance of a periodic motion by a steady or aperiodic energy supply. In a self-oscillator, the driving force is controlled by the oscillation itself so that it acts in phase with the oscillation, causing a negative damping that feeds energy into the oscillation. In contrast with driven oscillations, a self-oscillator itself sets the frequency and phase of the oscillations, keeping the frequency and phase for a number of periods.

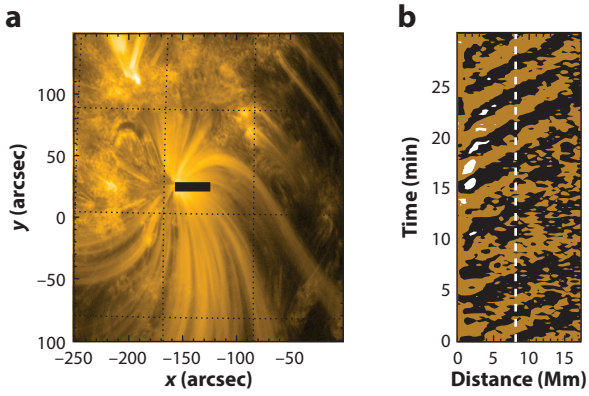

Figure 4

(*a*) EUV image of an active region, taken in the EUV band, with a magnetic fan loop system. A slit along one of the loops belonging to the fan is indicated with a black bar. (*b*) The time–distance map made for the slit directed along the bar. The time spans about ten cycles of the propagating periodic EUV disturbances. Adapted from Yuan & Nakariakov (2012). Abbreviation: EUV, extreme ultraviolet.

measurements of the propagation speed, using stereoscopic 3D observations. The estimation of the phase velocity inclination angle to the local normal and the true slow wave speed showed values of $37° \pm 6°$ and 132 ± 11 km s^{-1}, respectively, consistent with the interpretation in terms of slow waves.

Damping lengths of the EUV propagating disturbances are found to vary with the oscillation frequency (e.g., Krishna Prasad et al. 2014, Mandal et al. 2016a) and temperature (e.g., Krishna Prasad et al. 2012a,b, 2019), which again strengthens their interpretation as slow waves. More specifically, shorter damping lengths are detected for shorter-period oscillations that are observed in hotter wavebands. Using combined spectroscopic and stereoscopic imaging observations, Marsh et al. (2011) measured the damping length of slow wave–associated propagating disturbances in three dimensions and determined it to be about 20 Mm. Similar frequency-dependent dissipation lengths of propagating compressive waves in a polar coronal hole were detected by Gupta (2014). A change of the damping regime with height, from a rapid damping within the first 10 Mm of the detected wave propagation to a rather moderate (slow) damping at higher heights, was observed. This could indicate that different damping mechanisms dominate at different stages of the wave evolution and/or at different heights (see discussion in Section 2.3).

A quasi-periodic nature of the coronal slowly propagating intensity perturbations is likely determined by the conditions at the footpoints of the coronal waveguiding structures. Therefore, it would be natural to associate propagating coronal slow waves with the chromospheric oscillations, e.g., 3-min umbral oscillations, leaking into the corona (e.g., Botha et al. 2011). Indeed, analysis based on the time delays between intensity oscillation peaks observed in different wavelengths or spectral lines showed that slow waves can propagate from lower layers into the corona (e.g., Su et al. 2013, Deres & Anfinogentov 2015). The high monochromaticity of slow waves observed in the corona above sunspots is consistent with the high monochromaticity of 3-min umbral oscillations.

Substantially longer-period decaying propagating disturbances in coronal structures, with periods of a few tens of minutes, have been detected by Yuan et al. (2011) and Krishna Prasad et al. (2014) (see also Banerjee & Krishna Prasad 2016 for a review). Although the apparent phase speeds coincide with the local sound speed ($\sim$100 km s^{-1}), which allows the association of these intensity perturbations with slow modes, the physical nature of such long periodicities remains unclear.

6. STANDING AND SLOSHING SLOW OSCILLATIONS IN CORONAL LOOPS

6.1. Standing (SUMER) Oscillations

Standing slow magnetoacoustic oscillations in hot coronal loops[8] were first identified in the data obtained with the Solar Ultraviolet Measurements of Emitted Radiation (SUMER) spectrometer on the SOHO mission, after which standing slow oscillations are commonly known as SUMER oscillations (see Wang 2011 for a review). Oscillations of the SUMER class are manifested as decaying long-period (longer than a few minutes) harmonic variations of the Doppler shift and sometimes the emission intensity with a quarter-period phase lag. SUMER oscillations have been also detected with other instruments and in other wavebands at the emission lines associated with the formation temperatures ranging from 0.6 MK to 14 MK. In some cases, an unexpected increase in the decay time with temperature was detected (see Mariska 2006, Mariska & Muglach 2010; and see Section 2.3). Sometimes, SUMER oscillations are simultaneously detected in the Doppler shift and line-integrated intensity of the emission line, and also in soft X-ray flux and EUV light curves (Li et al. 2017).

Characteristic periods of SUMER oscillations are determined by the acoustic travel time along the loop and are found to range from about a few minutes to several tens of minutes. A collection of all SUMER oscillation events published in the research literature allowed for an effective multi-instrumental statistical analysis of such events (Nakariakov et al. 2019b). The use of the Markov chain Monte Carlo (MCMC[9]) technique revealed a clear scaling of the SUMER oscillation period with the temperature of the oscillating loop (see **Figure 1**). Clustering of data points around certain values of the temperature is attributed to the specific emission line formation temperatures of the instruments used for detections. Such a scaling could be associated with the decrease of the acoustic travel time with temperature, i.e., with the sound speed. In **Figure 1**, we show the best fit of the observed dependence with a model accounting for a $T^{-1/2}$ proportionality of the acoustic travel time with temperature, which is seen to be well consistent with the observed behavior. In contrast, this tendency could be also connected with a possible dependence of the loop length upon temperature (Wang 2011). However, a good agreement with the simple $T^{-1/2}$ model, where the loop length is assumed to be temperature-independent, does not make this assumption necessary.

Another prominent property of SUMER oscillations is that they are usually rapidly damped. The oscillation q-factor is typically about unity for SUMER oscillations (see **Figure 1**). The mechanisms for such damping, and their relative efficiency in certain physical conditions, as well as the dependence of the damping on the oscillation wavelength are still intensively debated. The lack of a commonly accepted damping mechanism stimulates both the revision of the standard damping mechanisms, such as by thermal conduction and viscosity, and the inclusion of new physical effects (see Section 2.3). In particular, one of the unresolved puzzles is that the SUMER oscillation damping time $\tau_{\rm D}^{\rm slow}$ scales with the oscillation period $P_{\rm slow}$ as $\tau_{\rm D}^{\rm slow} = a_0 P_{\rm slow}^{b_0}$ with $a_0 \approx 1.14^{+1.15}_{-0.5}$ and $b_0 \approx 0.91^{+0.2}_{-0.24}$ (see **Figure 1**). The uncertainties are estimated at the 95% confidence level. This empirically determined linear scaling is difficult to explain in terms of, in particular, viscous or conductive linear damping, where it is expected to have a quadratic form (see Banerjee & Krishna Prasad 2016, their table 1). Furthermore, Wang et al. (2015) empirically showed that in flaring conditions the observed damping rates of a SUMER oscillation could be reproduced in terms of

[8]Hot, warm, and cool coronal loops have temperatures of ∼10 MK, 1–2 MK, and <1 MK, respectively.

[9]The Markov chain construction is used for sampling a desired probability distribution in a multidimensional space of model parameters. This technique is widely involved in modern statistical approaches such as Bayesian analysis. In solar physics, MCMC is usually used for best fitting observational data sets by complex multi-parametric models and obtaining robust and reliable uncertainties.

a fundamental standing slow wave only with the thermal conductivity artificially suppressed by a factor of 3 from the Spitzer value or with the compressive viscosity enhanced by a factor of 15 from the Braginskii compressive viscosity. Such a detected discrepancy in the estimated and theoretical values of the transport coefficients suggests that neither of them are always a sufficient mechanism for the interpretation of the observed behavior of slow waves. It indicates the need for accounting for additional physical effects in the model, with a possible potential for new seismological inversions (see Sections 2.3 and 8.4 for detail).

SUMER oscillations should manifest nonlinear properties, as their amplitudes are typically large, exceeding ~10% of the local sound speed. Furthermore, a recent statistical survey showed that the q-factor of SUMER oscillations scales with the oscillation amplitude with the power-law index of $\sim -1/3$ (Nakariakov et al. 2019b), indicating the need for further development of nonlinear models for these oscillations and accounting for the corresponding nonlinear effects for adequate interpretation of observations. In particular, nonlinear effects may modify the scaling of the damping time with the oscillation period. A subtle point in establishing such a correlation between the oscillation q-factor and the velocity amplitude is the impact of the projection effect (see also the discussion of this effect in the context of kink oscillations in Section 4.2). Due to an unknown angle between the LoS and the direction of the plasma movements in the oscillation, the measured apparent velocity amplitude is always lower than the actual amplitude. In other words, for a given value of the q-factor, the maximum detected value of the velocity amplitude should be treated as the closest to an actual amplitude, thus making only the outer boundary of the observed data cloud in the (q-factor versus apparent amplitude) plane, not the entire cloud, meaningful.

6.2. Sloshing Oscillations

Another recently discovered and intensively studied observational manifestation of slow waves in coronal loops is the so-called sloshing oscillations. A sloshing oscillation is a slow wave bouncing back and forth along the loop and reflecting at the footpoints, with the density and velocity perturbations being either in phase or in antiphase. During the evolution, it shows no evidence of developing into a fundamental slow standing mode. They are directly observed by SDO/AIA as localized enhancements of the EUV emission intensity in hot coronal loops, bouncing back and forth between the footpoints (e.g., Kumar et al. 2013, 2015; Mandal et al. 2016b; Pant et al. 2017). By the analogy with water sloshing inside a container, Reale (2016) introduced the term sloshing for this phenomenon. Periods and damping times of sloshing oscillations are about several minutes, whereas the apparent propagation speed coincides with the sound speed in the loop. Similar to SUMER oscillations, this allows one to associate the coronal sloshings with the evolution of slow magnetoacoustic modes in closed magnetic configurations. In contrast to SUMER oscillations in which the density and velocity perturbations are quarter-period phase-shifted, these perturbations in sloshings are either in phase or in antiphase. This difference is deemed to be an intrinsic property of the sloshing oscillation, which is essentially a slow magnetoacoustic pulse propagating in a closed magnetic structure and reflecting at its boundaries, not a superposition of several standing parallel harmonics. This in turn suggests that at least some cases of SUMER oscillations reported in earlier works, in which the clear quarter-period phase shift between the intensity and velocity perturbations was not detected, could actually belong to the sloshing type of oscillations.

In the time–distance maps obtained along a curved slit roughly coinciding with the loop axis, a sloshing oscillation exhibits a zigzag pattern, with a nonzero intensity variation in the vicinity of the loop apex (see **Figure 5*a*,*b***). The presence or absence of the intensity variation at the apex is the difference between sloshing and SUMER oscillation. Due to the LoS effect,

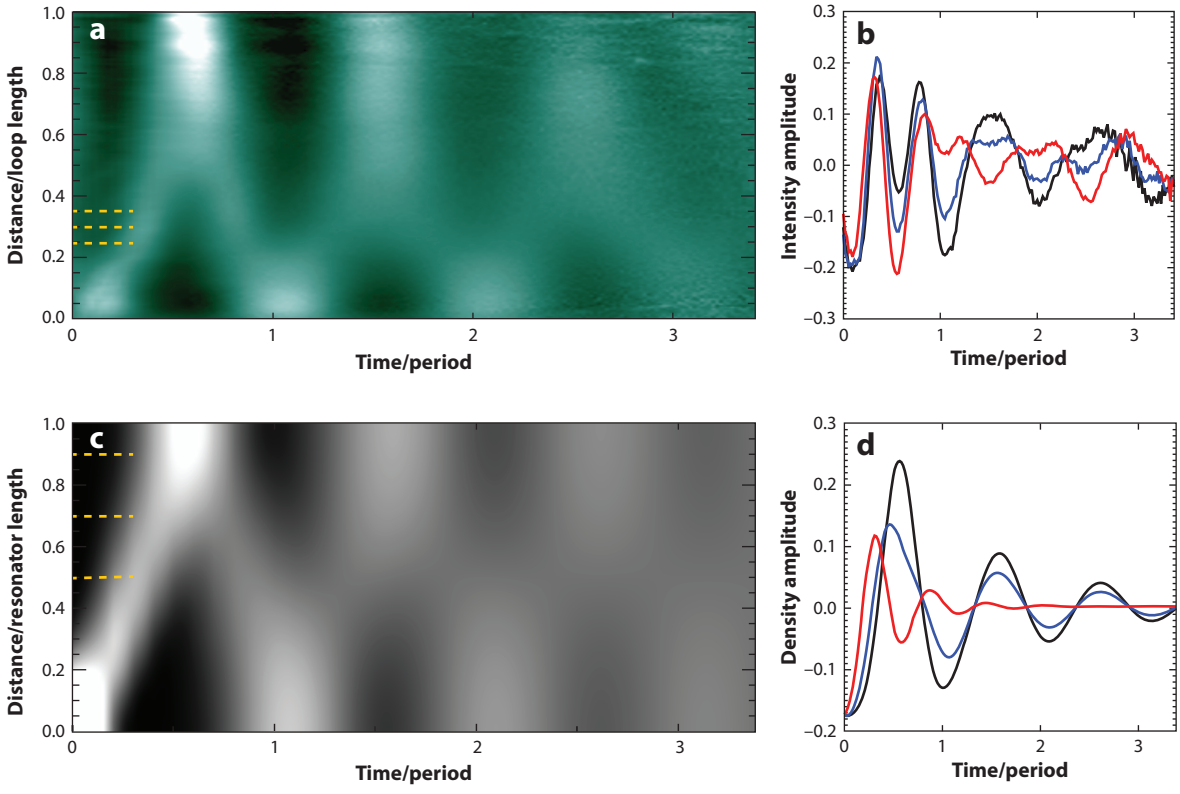

Figure 5

(*a*) Time–distance map of the sloshing event that occurred on May 7, 2012, observed by SDO/AIA at 94 Å (see Kumar et al. 2013, Nakariakov et al. 2019b). For each pixel, the global variation of the loop intensity with time was determined by smoothing and subsequent spline interpolation, which was then used for normalization of the original signal. The horizontal dashed bars indicate the pixels apparently situated near the loop apex. (*b*) Time variation of the normalized extreme-UV emission intensity near the apex, namely, at 0.25 (*red*), 0.3 (*blue*), and 0.35 (*black*) of the distance measured in the loop's length, shown in panel *a*. (*c*) Evolution of an acoustic Gaussian pulse in a one-dimensional resonator, obtained numerically with the linearized acoustic equations with viscous damping. The horizontal dashed bars indicate the pixels at which the time variation of the density, shown in panel *d*, are taken. (*d*) Time variation of the normalized density in the resonator at 0.5 (*red*), 0.7 (*blue*), and 0.9 (*black*) of the resonator length. Abbreviations: SDO, *Solar Dynamics Observatory*; AIA, Atmospheric Imaging Assembly.

the apparent trajectory of a sloshing pulse could be asymmetric, i.e., stretched toward one of the footpoints and squeezed toward the other, as shown in **Figure 5*a***, making identification of the loop apex position nontrivial. In the example shown in **Figure 5**, we assume the loop apex to be situated between 0.25 and 0.35 of the projected loop length and consider variation of the intensity within this interval. We compare the observed sloshing event with an expected behavior of an idealized broadband density splash in a 1D acoustic resonator (see **Figure 5*c,d***) modeled in terms of standard linear acoustics with viscous damping. Due to the wavelength-dependent energy dissipation, in this numerical example the initially broadband propagating pulse develops quickly into the fundamental standing mode with a clear node at the center of the resonator (cf. a similar density variation in Wang et al. 2018, their figure 12). However, for some as-yet-undefined reason the observed sloshing pulse does not degenerate with time into a fundamental slow harmonic but remains composed of several parallel harmonics, all of which decay at approximately the same rate (Nakariakov et al. 2019b). It could indicate the presence of some additional mechanism,

e.g., nonlinearity, counteracting more effective damping of higher harmonics by viscous and conductive mechanisms. Such a scenario is still to be modeled.

6.3. Possible Manifestation of Slow Waves in Solar and Stellar Flares

In addition to direct detections of slow waves in the solar corona in imaging and spectroscopic observations, the slow modes could also be responsible for long-period QPP in solar and stellar flares (e.g., Van Doorsselaere et al. 2016). The observational parameters of both solar and stellar QPP are seen to be broadly varying from event to event. Typical oscillation periods span from a fraction of a second up to several tens of minutes. Sometimes the oscillatory patterns are highly nonstationary: The amplitude could be rapidly decaying or have the form of beating or short wave trains; the signals could be almost harmonic or very anharmonic. Among such a variety of different types of QPPs, there is a certain class, which shows rapidly decaying harmonic signals with relatively long periods from a few minutes to several tens of minutes, that resemble SUMER oscillations (Nakariakov et al. 2019a).

There is an increasing number of detections of long-period (a few minutes or longer) QPPs of the SUMER type, i.e., possibly produced by slow waves. For example, quasi-periodic variations of the microwave emission, with the period growing from 2.5 to 5 min, were observed by Reznikova & Shibasaki (2011) with the Nobeyama Radioheliograph (NoRH). A 13-min oscillation of the microwave and EUV emission intensity with the decay time of ∼16 min was detected simultaneously with SDO/AIA and NoRH by Kim et al. (2012). Kupriyanova et al. (2014) observed a 2-min QPP of the thermal microwave emission in a solar flare. The detected pulsation was cophased along the entire emitting loop, suggesting it is the fundamental slow harmonic. Likewise, a fundamental slow mode in the microwave and X-ray emission during the decay phase of a flare was detected by Kupriyanova & Ratcliffe (2016) as a 1-min damped harmonic oscillation. The very long-period pulsations (8–30 min) of the soft X-ray emission detected before the onset of a flare could also be attributed to the evolution of a slow wave in the active region (Tan et al. 2016). More recently, the 4–5-min QPP of the thermal emission produced by the most powerful solar flare of cycle 24, on September 6, 2017 (SOL2017-09-06), was observed to exhibit properties compatible with SUMER oscillations (Kolotkov et al. 2018b). An 80-s QPP detected in the X-ray and microwave emission in a strong X1.0-class solar flare has been interpreted as the second harmonic of a standing slow wave in the flaring arcade (Kupriyanova et al. 2019). In addition, flaring light curves from magnetically active stars observed in the X-ray, white light, and UV bands were shown to have damped QPPs with the period from a few to several tens of minutes during the flare decay phase (e.g., Srivastava et al. 2013, Pugh et al. 2016, Doyle et al. 2018). Standing slow waves have been considered among potential mechanisms for a QPP with period of ∼11 min and damping time of ∼20 min, recently detected in the white light emission from a giant stellar flare (Jackman et al. 2019).

A comparative analysis of statistical properties of such SUMER-type QPPs, observed in the X-ray emission from solar and stellar flares by Cho et al. (2016), showed that their decay time $\tau_{\rm qpp}$ relates to the oscillation period $P_{\rm qpp}$ similarly to the dependence detected for SUMER oscillations (see Section 6.1). In **Figure 1**, this relation is approximated by a power-law function $\tau_{\rm qpp} = a_1 P_{\rm qpp}^{b_1}$ with $a_1 \approx 1.97^{+0.71}_{-0.52}$ and $b_1 \approx 0.94^{+0.08}_{-0.09}$, with the uncertainties estimated at 95% confidence level. Within the error bars, the power-law indices $b_0 \approx 0.91^{+0.2}_{-0.24}$ for SUMER oscillations and $b_1 \approx 0.94^{+0.08}_{-0.09}$ for X-ray QPPs are statistically identical. This evidence stands in favor of the attribution of the observed QPP to the dynamics of slow waves in the coronal plasma. Furthermore, this remains true for both solar and stellar QPPs, suggesting similarity between physical mechanisms operating in solar and stellar flares. However, **Figure 1** also shows

a substantial difference between the mean values of the other parameters of fitting, $a_0 \approx 1.14^{+1.15}_{-0.5}$ (for SUMER) and $a_1 \approx 1.97^{+0.71}_{-0.52}$ (for solar and stellar X-ray QPPs). Although they certainly overlap in the statistical sense within the estimated uncertainties, this difference could indicate the presence of an offset between these two data clouds. The difference could be caused, for example, by the specific mechanism for the production of the electromagnetic wave modulation by a slow mode, which is missing in this analysis. Another possible reason for the discrepancy could be connected with the artifacts of the data processing techniques. For example, in Mariska (2006), the SUMER oscillation (which occurred on October 7, 1991, and is included in the statistics shown in **Figure 1**) is found to have the oscillation q-factor of ~0.3, implying that the damping time could be underestimated. In **Figure 1**, we also show fitting of the entire data cloud combining statistics from Cho et al. (2016) for solar and stellar X-ray QPPs and from Nakariakov et al. (2019b) for SUMER oscillations. The best-fitting power-law function, $\tau_{\rm all} = a_2 P_{\rm all}^{b_2}$, with $a_2 \approx 1.42^{+0.15}_{-0.13}$ and $b_2 \approx 0.89^{+0.09}_{-0.05}$ and 95% confidence uncertainties, shows consistent results.

Coronal funnel-like (or fan) structures: plasma nonuniformities diverging radially or superradially outward from an active region; they are believed to be open-field magnetic flux tubes

7. QUASI-PERIODIC RAPIDLY PROPAGATING WAVE TRAINS

Signatures of rapidly propagating quasi-periodic wave trains of the EUV intensity disturbances are directly observed as spatially confined, arc-shaped quasi-periodic EUV emission disturbances rapidly propagating along coronal funnel-like structures (see **Figure 6**). Since the first unequivocal observation of such wave patterns (Liu et al. 2011), several detections were claimed, all reporting similar observational properties, i.e., the apparent phase speed of 500–2,200 km s^{-1}, oscillation periods of 1–3 min, and amplitudes up to several percent (see discussion in Liu et al. 2011 and Nakariakov et al. 2016b). Excitation of the wave trains was found to be connected with eruptions

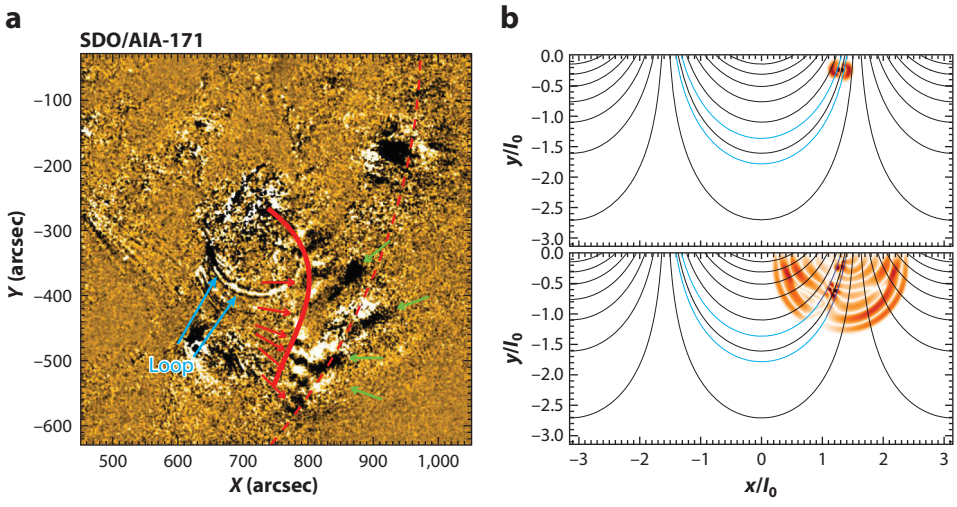

Figure 6

(*a*) Running-difference intensity image showing a snapshot of a propagating fast wave train seen as quasi-periodically spaced bright and dark regions (*red* and *green arrows*). The red solid and dashed lines show an apparent trajectory of the wave train and the solar limb, respectively. (*b*) Snapshots of the simulated progression of the absolute value of the induced flow velocity, taken at two instants of the computational time $\tilde{t} = 0.1$ (*top*) and 1 (*bottom*). The blue solid lines show the waveguiding coronal loop. l_0 is the normalization length scale. For example, for the characteristic wave speed of 1 Mm s^{-1} and timescale of 80 s, $l_0 = 80$ Mm. Adapted from Nisticò et al. (2014) with permission.

and/or flaring energy releases (e.g., Yuan et al. 2013). This phenomenon is clearly different from the slow waves discussed in Section 5, because in this wave process the phase speed is several times higher, and the occurrence is rather sporadic and induced by energy releases.

Ofman et al. (2011) demonstrated that the observed wave trains are fast waves. The quasi-periodicity could be attributed to a periodic driver as suggested by Liu et al. (2011). However, the observed periodicity could also result from an impulsive perturbation developing into a quasi-periodic wave train by the waveguide dispersion (Pascoe et al. 2013b). Because of the intrinsic period modulation of the fast wave trains created by a broadband pulse, their wavelet spectra may have characteristic tadpole features, with a narrowband tail and a broadband head (see **Supplemental Figure 4** of the **Supplemental Text**). The dominant periodicity and the wave train duration are determined by the conditions inside and outside the waveguiding plasma nonuniformity, as well as by the duration of the propagation (Oliver et al. 2015). The formation of both trapped and leaky counterparts of a fast wave train, predicted theoretically, was detected by Nisticò et al. (2014). Pascoe et al. (2017) showed that the waveguide dispersion suppresses the nonlinear steepening in the trapped wave trains, whereas individual wave cycles in the leaky wave trains are subject to steepening and shock formation. This theoretical result is found to be consistent with the detection of two counter-propagating fast wave trains from neighboring active regions (Ofman & Liu 2018). Direct comparison of observations with the 3D MHD modeling provides an interesting possibility for the analysis of linear and nonlinear interactions in fast waves.

Supplemental Material >

In addition to direct observations in the EUV, characteristic signatures of dispersively evolving fast wave trains have been indirectly inferred by the quasi-periodic modulation of radio emission, such as solar radio bursts.[10] For example, Mészárosová et al. (2009) observed tadpole features in wavelet spectra of type IV radio bursts. Fast wave train signatures were also found in radio fiber bursts and spikes (see Karlický et al. 2013, and references therein). Goddard et al. (2016) and Kumar et al. (2017) reported simultaneous detection of quasi-periodic EUV and radio emission disturbances with similar repetition rates. Quasi-periodic striation in the fine structure of a radio burst was associated with a fast wave train by Kolotkov et al. (2018a).

8. MAGNETOHYDRODYNAMIC SEISMOLOGY

The dependence of observable properties of MHD waves, such as temporal and spatial spectra, phase and group speeds, phase relations between perturbations of different physical quantities, etc., allows for probing parameters of the waveguiding plasma. This approach, suggested for the diagnostics of corona plasma nonuniformities by local MHD oscillations by Roberts et al. (1984), is known as MHD seismology. Similar techniques used for diagnostics of a plasma in controlled fusion devices and in the Earth's and planetary magnetospheres are known as MHD spectroscopy (e.g., Fasoli et al. 2002) and magnetoseismology (e.g., Chi et al. 2009), respectively. The latter term is sometimes used for coronal seismology too, as well as for chromospheric seismology. MHD seismology allows for obtaining estimates of several key parameters of the coronal plasma.

8.1. The Alfvén Speed and Magnetic Field by Kink Oscillations

Since their first detection, kink oscillations of coronal loops have been used for probing the Alfvén speed and absolute value of the magnetic field in the oscillating loop, following the technique

[10]Solar radio bursts are sporadic increases in the solar radio emission, associated with solar flares or coronal mass ejections. Depending upon characteristic spectral signatures, different types of solar radio bursts are distinguished (e.g., Dulk 1985).

designed by Nakariakov & Ofman (2001). As the observations show that the kink oscillation is a standing fundamental harmonic of the kink mode of the loop, the wavelength could be taken as double the length of the loop. Under the assumption of a semicircular shape, the loop length could be estimated by the distance between the footpoints with the correction for the projection effect or by the height of the loop apex above the surface. When quasi-stereoscopic observations of the corona are available, the 3D geometry of the oscillating loop could be determined more rigorously (e.g., Verwichte et al. 2013; see also Section 8.6). The oscillation period could be readily determined from the time–distance map showing the transverse displacement of the loop. The ratio of the wavelength to the oscillation period gives us the phase speed. As the wavelength is usually a few hundred times greater than the loop's minor radius, the phase speed is approximately equal to the kink speed. In a low-β plasma of coronal active regions, the kink speed is determined by the Alfvén speed and the density ratio outside and inside the loop. The density ratio could be estimated by the contrast of the loop brightness in an EUV channel, though this estimation is subject to serious uncertainties connected with the optically thin nature of the observed emission. Both the brightnesses inside and outside the loop contain the contribution of the plasma emission in front of and behind the loop, integrated along the LoS. The density ratio requires the knowledge of the ratio of the intensities of the emission from an LoS passing through the loop and near it and does not require the absolute values of the intensities. Thus, one obtains the estimations of the external and internal Alfvén speeds as

$$C_{\mathrm{A0}} \approx C_{\mathrm{K}}/\sqrt{2/(1+\rho_{\mathrm{e}}/\rho_{\mathrm{i}})}, C_{\mathrm{A_e}} \approx C_{\mathrm{A0}}/\sqrt{\rho_{\mathrm{e}}/\rho_{\mathrm{i}}}, \qquad 9.$$

respectively (e.g., Nakariakov & Ofman 2001). If there is an independent estimate of the density of the plasma, e.g., by spectroscopy, the value of the Alfvén speed allows us to estimate the absolute value of the magnetic field. In particular, inside the loop it is $B_0 \approx C_{\mathrm{A0}}(\mu\rho_0)^{1/2}$. The credibility of this technique was demonstrated by Verwichte et al. (2013) by comparing coronal seismology results with the results obtained by the extrapolation of the photospheric magnetic field. In this method, the main source of error is the uncertainty in the estimation of the plasma density. However, as it appears in the expression for the magnetic field under the sign of the square root, the corresponding error in the magnetic field is fortunately reduced by a factor of two.

The estimation of the Alfvén speed could be affected by the variation of the plasma density along the loop, caused by stratification, and the variation of the minor radius of the loop. In particular, for the loops filled in with a plasma with the temperature of ~1 MK, the hydrostatic density scale height is ~50 Mm, which is about the loop's major radius. This effect is slightly reduced by the inclination of the plane of the loop from the vertical direction. The dependence of the ratio of the oscillation periods associated with different parallel harmonics on the longitudinal nonuniformity of the magnetic field and/or density, allows for the seismological estimation of those dependencies (e.g., Andries et al. 2009). In the long-wavelength limit, for example, for several lowest-standing parallel kink harmonics, the effect of longitudinal nonuniformity is accounted for by Equation 5. The field variation along the loop can be quantified by the ratio of the minor radii near the apex, r_{apex}, and footpoints, r_{fp}, $\Gamma = r_{\mathrm{apex}}/r_{\mathrm{fp}}$. Assuming a constant equilibrium density, Verth & Erdélyi (2008) showed that Γ could be estimated by the ratio of the periods of the lowest parallel harmonics,

$$\Gamma^2 \approx 1 + \frac{2\pi^2}{3}\left(\frac{P^{(1)}_{\mathrm{kink}}}{2P^{(2)}_{\mathrm{kink}}} - 1\right). \qquad 10.$$

In coronal loops with a constant cross section, the value of the magnetic field should be constant at any height, and the kink speed, $C_{\mathrm{K}}(z)$, remains the only unknown function in Equation 5,

allowing for its inversion from observations. Ruderman et al. (2016) demonstrated that the ratio $P^{(1)}_{\rm kink}/2P^{(2)}_{\rm kink}$ is a monotonically increasing function of the ratio of the kink speeds at the loop top and near footpoints. When the kink speed increases with height, $P^{(1)}_{\rm kink}/2P^{(2)}_{\rm kink} < 1$, whereas $P^{(1)}_{\rm kink}/2P^{(2)}_{\rm kink} > 1$ when the kink speed decreases with height.

An important advantage of this seismological technique is the clear association of the diagnostics with a certain plasma structure, which makes the estimation of the Alfvén speed and magnetic field free of the LoS integration shortcomings intrinsic to the direct methods. Furthermore, seismology allows for estimating the field in off-limb regions where the field could not be determined by extrapolation. A promising future avenue is the application of this seismological technique with the use of decayless kink oscillations (Anfinogentov & Nakariakov 2019). As those oscillations are well detected during the quiet periods of time, the seismology based on them would allow us to get information about active regions before flares and mass ejections. It would be interesting to seek possible precursors of the energy releases in the behavior of decayless kink oscillations. The next step could be the development of seismological estimations of the free magnetic energy available in the active region by properties of the oscillations.

8.2. The Internal Structure of a Loop by Decaying Kink Oscillations

The steepness of the radial density profile in a kink oscillating loop could be obtained from its role in the damping rate, shown by Equation 3 (Pascoe et al. 2013a). In this approach, the observed rapid damping of an impulsively excited kink oscillation can be approximated with the expression in Equation 3, which gives us the observables $\tau_{\rm G}$, $\tau_{\rm exp}$, and $t_{\rm s}$. Pascoe et al. (2016a) performed first seismological inversions for the radial density profile and contrast ratio with the use of these characteristic times and obtained $\rho_{\rm i}/\rho_{\rm e} \approx 1.5$–$5$ and $l_{\rm rl}/a \approx 0.2$–1; i.e., the inhomogeneous layer width is comparable with the minor radius of the loop. This technique could highly benefit from the independent estimation of the $l_{\rm rl}/a$ by the direct comparison of the EUV intensity radial profile of the loop with forward modeling (e.g., Pascoe et al. 2018). Another promising improvement of the seismology is provided by the application of Bayesian analysis (see Arregui 2018 for a review), in particular, applying the MCMC sampling (e.g., Pascoe et al. 2018, 2019).

8.3. Partition of the Energy Released by a Flare by Kink Oscillations

In the scenario, when a decaying kink oscillation is excited by a blast wave generated by a flare occurring nearby, the initial amplitude of the oscillation would depend on the energy released by the flare (e.g., Ballai 2007). Estimating numerically the efficiency of the kink oscillation excitation by a pulse of the total pressure increase, localized at a certain distance from the loop, Terradas (2009) found that only about one one-millionth of the pulse energy goes to the kink oscillation. Estimating the energy of an observed kink oscillation (see Section 4), one can assess the energy of the pulse. Comparing this energy with the other kinds of energy released by the flare, one could estimate the part of the total flare energy that goes to the excitation of waves. Terradas (2009) suggested that this energy is comparable with other sinks of the released energy. Perhaps, the efficiency of the kink oscillation excitation by a pulse may also depend on the density contrast between the loop and its surrounding, the loop's mass, the location of the pulse with respect to the loop, the nature of the pulse itself, and its duration, etc. This could be the subject of further research.

8.4. The Polytropic Index and Thermal Conductivity by Slow Oscillations

The sensitivity of slow magnetoacoustic waves to thermodynamical parameters of the plasma, in particular, the dependence of the sound and tube speeds on the plasma temperature and the

polytropic index, can be used for seismological probing of these parameters. In a sound wave, the relative perturbations of the density and temperature, $\tilde{T}/T_0$ and $\tilde{\rho}/\rho_0$, are linked with each other and with the polytropic index, $\gamma_{\rm eff}$, and the thermal conductivity coefficient, κ, as

$$\frac{\tilde{T}}{T_0} = \frac{\tilde{\rho}}{\rho_0}(\gamma_{\rm eff} - 1)\cos\Delta\phi, \qquad \tan\Delta\phi = \frac{\pi m_{\rm p}(\gamma_{\rm eff} - 1)\kappa}{k_{\rm B} c_{\rm s}^2 P \rho_0}, \qquad 11.$$

where the phase difference $\Delta\phi = (\Delta t/P) \times 360$ is the time lag between the density and temperature perturbations, with Δt measured in the oscillation periods P (e.g., Krishna Prasad et al. 2018), and $m_{\rm p}$ is the proton mass. Thus, obtaining $\tilde{T}/T_0$ and $\tilde{\rho}/\rho_0$, and the phase shift $\Delta\phi$ between them observationally, reduces the number of unknown variables in Equation 11 to two, namely $\gamma_{\rm eff}$ and κ, whose values could be estimated seismologically. In the limiting case of a nearly isothermal plasma dominated by thermal conduction with $\gamma_{\rm eff} \to 1$, any temperature perturbations are smoothed out along the loop; i.e., $\tilde{T}/T_0 \to 0$. Likewise, in an approximately adiabatic case with $\gamma_{\rm eff} \approx 5/3$ and negligible thermal conduction, $\Delta\phi \to 0$; i.e., the density and temperature perturbations are in phase with each other, and their relative amplitudes relate as 2/3. Note, however, that the expressions in Equation 11 do not account for other nonadiabatic effects, such as thermal misbalance, and nonlinear effects, which could also modify the effective polytropic index, $\gamma_{\rm eff}$ (see Zavershinskii et al. 2019) and the phase shift, $\Delta\phi$.

Van Doorsselaere et al. (2011b) used spectroscopic measurements of the relationship between relative density and temperature perturbations in propagating slow waves in a coronal fan to estimate the effective polytropic index. Using the polytropic assumption, i.e., not accounting for the phase shifts between density and temperature perturbations, $\gamma_{\rm eff}$ was estimated as 1.10 ± 0.02. Accounting for finite thermal conductivity yielded $\gamma_{\rm eff} \approx 1.17$. Wang et al. (2015) used observations of temperature and density perturbations in a standing slow wave in a hot loop and got the estimation $\gamma_{\rm eff} = 1.64 \pm 0.08$. Such a value of $\gamma_{\rm eff}$ could be interpreted as either the indication of a suppression of the Spitzer thermal conductivity by at least a factor of ~3 or an increase in the classical compressive viscosity by up to a factor of 15. A physical reasoning for such a modification of the transport coefficients requires further investigation. Krishna Prasad et al. (2018) estimated $\Delta\phi \approx 120°$ in propagating slow waves and concluded that $\gamma_{\rm eff}$ increases with temperature from 1.04 ± 0.01 to 1.58 ± 0.12. Such a positive correlation between $\gamma_{\rm eff}$ and temperature cannot be explained by the effect of thermal conduction, for which $\gamma_{\rm eff}$ decreases with temperature from ~5/3 in the adiabatic regime to approximately 1 in the isothermal regime, indicating the need to account for additional nonadiabatic effects in Equation 11.

8.5. The Alfvén Speed and Magnetic Field by Slow Oscillations

In a finite β plasma, slow waves become sensitive to the magnetic field, allowing for its seismological diagnostics. Associating the observed phase speed of the slow wave with the tube speed, $C_{\rm T}$, and obtaining the sound speed, $C_{\rm s}$, from the line formation temperature, the plasma β can be estimated as

$$\beta = 2\gamma_{\rm eff}^{-1}\left[(C_{\rm s}/C_{\rm T})^2 - 1\right]. \qquad 12.$$

Wang et al. (2007) analyzed seven Doppler shift oscillation events detected in the hot flare line Fe XIX, which were interpreted in terms of fundamental standing slow waves. The physical parameters of the oscillating loops, such as geometry, temperature, and electron density, were obtained from contemporaneous multichannel, soft X-ray imaging observations. This allowed for the estimation of the magnetic field in the loops, based on Equation 12. For the seven events considered,

the plasma β was found in the range of 0.15–0.91 with a mean of 0.33 ± 0.26, allowing the magnetic field to be 34 ± 14 G. Correction to the background emission reduces this estimation by 9–35%, giving 22 ± 13 G as the lower limit. A similar approach was applied by Jess et al. (2016) to slow waves leaking from sunspots. The plasma density and temperature estimates for the coronal region above the sunspot and its locality were obtained by the differential emission measure (DEM) technique. Interpreting the observed phase speed as the tube speed, the coronal magnetic field decreased rapidly with the radial distance from the center of the underlying sunspot from 32 ± 5 G to 1 G. A simultaneous observation of a fast wave train (see Section 7) and slow waves (see Section 5) propagating apparently along the same plasma structure constrains the product of the plasma β and the polytropic index, γ_{eff}, in the oscillating loop: $\gamma_{\text{eff}}\beta = 2(C_s/C_A)^2$. Zhang et al. (2015) estimated this product as 0.015.

Differential emission measure (DEM): an observable characterizing coronal optically thin emission intensity at a given temperature and for the total plasma density along the LoS

8.6. Magnetic Field Geometry

In the absence of instruments that provide us with stereoscopic or, at least, quasi-stereoscopic observations of the corona, an intrinsic observational difficulty is the lack of knowledge about the local direction of the coronal magnetic field and, more generally, its 3D geometry. Some information can be obtained by dynamic stereoscopy, which is based on the observation of a coronal plasma structure from different angles due to solar rotation. However, this method is only applicable to the long-lived magnetic configurations that do not evolve during at least a few days.

Another approach is the determination of the coronal magnetic field geometry by the extrapolation of the magnetic field measured at the photosphere, which can be applied to plasma structures at the central part of the solar disk. The confinement of the propagation direction of slow waves to the magnetic field (Section 2.3) could be used for revealing the local direction of the field with respect to the LoS. The plausibility of such a seismological application has been demonstrated by Marsh et al. (2009), who used the then-available stereoscopic information about the magnetic field direction and showed that the phase speed of slow waves is indeed consistent with theoretical estimations. However, the application of this technique requires the knowledge of the plasma temperature and polytropic index. Propagating fast wave trains (Section 7) could be used for the same purpose (e.g., Ofman et al. 2011), but in that case the observed wave patterns must correspond to the guided, rather than leaky, part of the wave.

8.7. Flaring Site Plasmas and Fields by Sausage Oscillations

Parameters of sausage oscillations manifested as QPP modulating the microwave emission in flares can provide useful seismological information. In particular, the phase speed of long-wavelength trapped sausage oscillations, determined by the loop length L and oscillation period P, gives us the estimation of the external Alfvén speed, $C_{A_e} \approx 2L/P_{\text{saus}}$, which is difficult to measure otherwise. In the leaky regime, the sausage oscillation period is linked with the internal Alfvén speed C_{A_i} as $P_{\text{saus}} \approx 2.6a/C_{A_i}$, and the additional observable is the q-factor, $\approx \pi^{-2}(\rho_i/\rho_e)$ (see Section 3 and Kopylova et al. 2007). Tian et al. (2016) obtained a lower limit of the Alfvén speed outside an oscillating loop as $\sim$2.4 Mm s^{-1}, and the density contrast as larger than 40, by the analysis of sausage oscillations.

The sensitivity of P_{saus} and the leaky damping time to the steepness of the radial density profile adds another unknown parameter representing the steepness, which can be also expressed via the width of the transition layer l_{tr}. Chen et al. (2015b) designed a seismological inversion scheme and demonstrated that even in the lack of spatial information, the parameters describing the loop, a/C_{A_i}, l_{tr}/a, and ρ_i/ρ_e, could be well constrained.

Flaring loops in which sausage oscillations are usually detected could be twisted. Without the twist, in a low-β plasma, the parallel magnetic field inside and outside the loop has similar values. As the internal Alfvén speed C_{A_i} can be estimated by the magnetic field and density obtained from the gyrosynchrotron spectrum (Melnikov et al. 2005), the ratio C_{A_e}/C_{A_i} gives the external plasma density. If the density contrast is estimated independently, the discrepancy of the directly and seismologically estimated density contrast ratios should be attributed to the effect of the magnetic twist. Thus, it might be possible to seismologically estimate the magnetic twist and the associated nonpotential magnetic energy. This approach could be generalized on the case of finite β. In addition, one can use Equation 2 linking the damping time with the magnetic twist.

Simultaneous observation of fundamental sausage and kink modes could strongly improve the seismological inversion (Guo et al. 2016). Likewise, the simultaneous observation of slow oscillations (of the SUMER kind) and sausage oscillations with the periods $P_{\rm slow}$ and $P_{\rm saus}$ imposes the important constraint on the values of the plasma β and polytropic index γ in the oscillating loop surrounded by a zero-β plasma (Van Doorsselaere et al. 2011a),

$$\frac{P_{\rm slow}}{P_{\rm saus}} \approx (1+\beta)\frac{\rho_{\rm i}}{\rho_{\rm e}}\left(\frac{2}{\gamma\beta}+1\right); \qquad 13.$$

see also Section 8.5 for the seismological potential of slow waves.

SUMMARY POINTS

1. The observational study and theoretical modeling of magnetohydrodynamic (MHD) wave processes in the solar corona are a mature, but still rapidly developing, research topic. The main observational progress has been accomplished owing to new-generation instruments providing high spatial and temporal resolution observations. Periods and wavelengths of kink and slow modes are confidently resolved in the extreme-UV (EUV) band, whereas those of shorter-period sausage modes are resolved in the microwave band. In addition, MHD modes of all kinds could be manifested as quasi-periodic pulsations modulating flaring emission.
2. The model based on MHD modes of a plasma cylinder remains a robust theoretical starting point for the interpretation of observations. An important feature of this model is its ability to not only successfully reproduce observed phenomena but also predict new ones; i.e., solar coronal wave studies are often theory driven. The model has demonstrated great potential for various generalizations addressing additional physical effects.
3. Major progress has been reached in understanding mechanisms for the excitation of some types of MHD waves, in both the theoretical modeling and observational validation. The dominating excitation mechanism for decaying kink oscillations is their displacement from the equilibrium by eruptions of magnetized plasma. Propagating slow waves are attributed to the leakage of chromospheric oscillations. Fast wave trains could be formed by the evolution of an initial impulsive perturbation caused by the waveguide dispersion. The recently appreciated activity of the coronal plasma, i.e., the thermal misbalance caused by compressive MHD waves, strongly affects the slow wave dynamics.
4. The determination of statistical scalings of various observables for the validation or rejection of theoretical models offers a powerful avenue for revealing physical mechanisms responsible for the behavior of different MHD modes. The linear scaling of kink

oscillation periods with the loop length clearly indicates their nature as kink eigenmodes of the loop. Damping of decaying kink and standing slow oscillations depends on the oscillation amplitudes. There are theoretical models that attribute the damping to nonlinear effects, e.g., based on the Kelvin–Helmholtz instability of a resonant layer and nonlinear parallel cascade.

5. High-precision observations of MHD waves, combined with elaborated theory, provide solid ground for seismological probing and constraining important parameters of the waveguiding plasma structures, such as the Alfvén speed, the absolute value of the magnetic field, stratification, plasma temperature, fine structuring, 3D geometry of coronal magnetic fields, polytropic index, field-aligned thermal conductivity, and coronal heating function.

FUTURE ISSUES

1. There is a great potential in the use of the omnipresent MHD oscillations for seismological diagnostics of the key parameters of the corona. A promising seismological tool offered by the ubiquitous decayless kink oscillations allows for probing parameters of active regions, in particular, before eruptive energy releases. An important future avenue is the development of seismological methods for the estimation of the nonpotential magnetic field and the free magnetic energy. The dependence of compressive oscillations such as slow modes on the coronal heating function provides us with a tool for its diagnostics and constraining. The effectiveness of MHD seismology can be strongly improved by the use of phase relations between different physical properties perturbed by the wave and by simultaneous observation of several different modes. In addition, there is a huge potential in the combination of seismological techniques with more traditional methods of the plasma diagnostics.
2. There is a need for developing nonlinear models for the damping of kink and slow modes, with the aim of explaining the statistically established power-law dependences of their q-factors on the relative amplitude, A, i.e., the $A^{-2/3}$ dependence for kink oscillations, and $A^{-1/3}$ for slow oscillations. In addition, coronal MHD wave models should include transport mechanisms based on the plasma turbulence. Forward modeling of instrument-specific observables is of high importance too. One of the highly demanded outcomes of the modeling is the production of scaling laws of various observables, which could be tested observationally.
3. As the apparent thermal equilibrium of the coronal plasma is sustained by the competition of cooling and (yet unknown) heating processes, MHD waves can readily cause a thermal misbalance. The back reaction of the thermal misbalance can be manifested as enhanced or suppressed damping or overstability, and wave dispersion. Thus, in theoretical modeling of coronal MHD waves it is important to include the heating function and its perturbations by the waves.
4. Analysis of sausage oscillations remains sporadic and would clearly benefit from a statistical study similar to those that have already been successfully performed for kink and slow modes. The direct dependence of sausage modes on the transverse profile of the plasma and independence of the plasma β and of the loop length (in the leaky regime) have promising seismological potential.

DISCLOSURE STATEMENT

The authors are not aware of any affiliations, memberships, funding, or financial holdings that might be perceived as affecting the objectivity of this review.

ACKNOWLEDGMENTS

This work was supported by the Science and Technology Facilities Council consolidated grant ST/T000252/1. V.M.N. acknowledges support from the BK21 PLUS program through the National Research Foundation funded by the Ministry of Education of Korea, and the Russian Foundation for Basic Research grant no. 18-29-21016. D.Y.K. acknowledges the budgetary funding of Basic Research program II.16.

LITERATURE CITED

Afanasyev AN, Nakariakov VM. 2015. *Astron. Astrophys.* 573:A32
Allian F, Jain R, Hindman BW. 2019. *Ap. J.* 880:3
Andries J, van Doorsselaere T, Roberts B, et al. 2009. *Space Sci. Rev.* 149:3–29
Anfinogentov SA, Nakariakov VM. 2019. *Ap. J. Lett.* 884:L40
Anfinogentov SA, Nakariakov VM, Nisticò G. 2015. *Astron. Astrophys.* 583:A136
Antolin P, De Moortel I, Van Doorsselaere T, Yokoyama T. 2016. *Ap. J. Lett.* 830:L22
Antolin P, De Moortel I, Van Doorsselaere T, Yokoyama T. 2017. *Ap. J.* 836:219
Antolin P, Pagano P, De Moortel I, Nakariakov VM. 2018. *Ap. J. Lett.* 861:L15
Antolin P, Van Doorsselaere T. 2013. *Astron. Astrophys.* 555:A74
Arregui I. 2015. *Philos. Trans. R. Soc. Lond. Ser. A* 373:20140261
Arregui I. 2018. *Adv. Space Res.* 61:655–72
Arregui I, Oliver R, Ballester JL. 2012. *Living Rev. Solar Phys.* 9:2
Aschwanden MJ. 2006. *Philos. Trans. R. Soc. Lond. Ser. A* 364:417–32
Ballai I. 2007. *Solar Phys.* 246:177–85
Banerjee D, Gupta GR, Teriaca L. 2011. *Space Sci. Rev.* 158:267–88
Banerjee D, Krishna Prasad S. 2016. *AGU Geophys. Monogr. Ser.* 216:419–30
Botha GJJ, Arber TD, Nakariakov VM, Zhugzhda YD. 2011. *Ap. J.* 728:84
Bradshaw SJ, Emslie AG, Bian NH, Kontar EP. 2019. *Ap. J.* 880:80
Carley EP, Hayes LA, Murray SA, et al. 2019. *Nat. Commun.* 10:2276
Chen PF. 2011. *Living Rev. Solar Phys.* 8:1
Chen SX, Li B, Xia LD, Yu H. 2015a. *Solar Phys.* 290:2231–43
Chen SX, Li B, Xiong M, Yu H, Guo MZ. 2015b. *Ap. J.* 812:22
Chen SX, Li B, Xiong M, Yu H, Guo MZ. 2016. *Ap. J.* 833:114
Chi PJ, Russell CT, Ohtani S. 2009. *Geophys. Res. Lett.* 36:L08107
Cho IH, Cho KS, Nakariakov VM, Kim S, Kumar P. 2016. *Ap. J.* 830:110
Claes N, Keppens R. 2019. *Astron. Astrophys.* 624:A96
Cranmer SR, Winebarger AR. 2019. *Annu. Rev. Astron. Astrophys.* 57:157–87
De Moortel I. 2009. *Space Sci. Rev.* 149:65–81
De Moortel I, Browning P. 2015. *Philos. Trans. R. Soc. Lond. Ser. A* 373:20140269
De Moortel I, Hood AW. 2003. *Astron. Astrophys.* 408:755–65
De Moortel I, Hood AW. 2004. *Astron. Astrophys.* 415:705–15
De Moortel I, Hood AW, Gerrard CL, Brooks SJ. 2004. *Astron. Astrophys.* 425:741–52
De Moortel I, Nakariakov VM. 2012. *Philos. Trans. R. Soc. Lond. Ser. A* 370:3193–216
De Moortel I, Pascoe DJ. 2012. *Ap. J.* 746:31
Deres AS, Anfinogentov SA. 2015. *Astron. Rep.* 59:959–67
Doyle JG, Shetye J, Antonova AE, et al. 2018. *MNRAS* 475:2842–51
Duckenfield T, Anfinogentov SA, Pascoe DJ, Nakariakov VM. 2018. *Ap. J. Lett.* 854:L5

Dulk GA. 1985. *Annu. Rev. Astron. Astrophys.* 23:169–224
Dymova MV, Ruderman MS. 2005. *Solar Phys.* 229:79–94
Edwin PM, Roberts B. 1983. *Solar Phys.* 88:179–91
Fang X, Yuan D, Van Doorsselaere T, Keppens R, Xia C. 2015. *Ap. J.* 813:33
Fasoli A, Testa D, Sharapov S, et al. 2002. *Plasma Phys. Control. Fus.* 44:B159–72
Giagkiozis I, Goossens M, Verth G, Fedun V, Van Doorsselaere T. 2016. *Ap. J.* 823:71
Goddard CR, Antolin P, Pascoe DJ. 2018. *Ap. J.* 863:167
Goddard CR, Nisticò G, Nakariakov VM, Zimovets IV, White SM. 2016. *Astron. Astrophys.* 594:A96
Goossens M, Andries J, Soler R, et al. 2012. *Ap. J.* 753:111
Goossens M, Erdélyi R, Ruderman MS. 2011. *Space Sci. Rev.* 158:289–338
Gosain S. 2012. *Ap. J.* 749:85
Gruszecki M, Nakariakov VM, Van Doorsselaere T. 2012. *Astron. Astrophys.* 543:A12
Guo M, Van Doorsselaere T, Karampelas K, et al. 2019. *Ap. J.* 870:55
Guo MZ, Chen SX, Li B, Xia LD, Yu H. 2016. *Solar Phys.* 291:877–96
Gupta GR. 2014. *Astron. Astrophys.* 568:A96
Gupta GR, Banerjee D, Teriaca L, Imada S, Solanki S. 2010. *Ap. J.* 718:11–22
Hindman BW, Jain R. 2008. *Ap. J.* 677:769–80
Hindman BW, Jain R. 2014. *Ap. J.* 784:103
Hood AW, Ruderman M, Pascoe DJ, et al. 2013. *Astron. Astrophys.* 551:A39
Howson TA, De Moortel I, Antolin P. 2017. *Astron. Astrophys.* 602:A74
Huang Z, Mou C, Fu H, et al. 2018. *Ap. J. Lett.* 853:L26
Ibanez S, Miguel H, Escalona T, Orlando B. 1993. *Ap. J.* 415:335–41
Inglis AR, van Doorsselaere T, Brady CS, Nakariakov VM. 2009. *Astron. Astrophys.* 503:569–75
Jackman JAG, Wheatley PJ, Pugh CE, et al. 2019. *MNRAS* 482:5553–66
Jess DB, Morton RJ, Verth G, et al. 2015. *Space Sci. Rev.* 190:103–61
Jess DB, Reznikova VE, Ryans RSI, et al. 2016. *Nat. Phys.* 12:179–85
Kaneda K, Misawa H, Iwai K, et al. 2018. *Ap. J. Lett.* 855:L29
Karampelas K, Van Doorsselaere T. 2018. *Astron. Astrophys.* 610:L9
Karlický M, Mészárosová H, Jelínek P. 2013. *Astron. Astrophys.* 550:A1
Kiddie G, De Moortel I, Del Zanna G, McIntosh SW, Whittaker I. 2012. *Solar Phys.* 279:427–52
Kim S, Nakariakov VM, Shibasaki K. 2012. *Ap. J. Lett.* 756:L36
Klimchuk JA. 2015. *Philos. Trans. R. Soc. Lond. Ser. A* 373:20140256
Kohutova P, Verwichte E. 2018. *Astron. Astrophys.* 613:L3
Kolotkov DY, Nakariakov VM, Kontar EP. 2018a. *Ap. J.* 861:33
Kolotkov DY, Nakariakov VM, Zavershinskii DI. 2019. *Astron. Astrophys.* 628:A133
Kolotkov DY, Pugh CE, Broomhall AM, Nakariakov VM. 2018b. *Ap. J. Lett.* 858:L3
Konkol P, Murawski K, Lee D, Weide K. 2010. *Astron. Astrophys.* 521:A34
Kopylova YG, Melnikov AV, Stepanov AV, Tsap YT, Goldvarg TB. 2007. *Astron. Lett.* 33:706–13
Krishna Prasad S, Banerjee D, Singh J. 2012a. *Solar Phys.* 281:67–85
Krishna Prasad S, Banerjee D, Van Doorsselaere T. 2014. *Ap. J.* 789:118
Krishna Prasad S, Banerjee D, Van Doorsselaere T, Singh J. 2012b. *Astron. Astrophys.* 546:A50
Krishna Prasad S, Jess DB, Van Doorsselaere T. 2019. *Front. Astron. Space Sci.* 6:57
Krishna Prasad S, Raes JO, Van Doorsselaere T, Magyar N, Jess DB. 2018. *Ap. J.* 868:149
Kumar P, Innes DE, Inhester B. 2013. *Ap. J. Lett.* 779:L7
Kumar P, Nakariakov VM, Cho KS. 2015. *Ap. J.* 804:4
Kumar P, Nakariakov VM, Cho KS. 2017. *Ap. J.* 844:149
Kupriyanova EG, Kashapova LK, Van Doorsselaere T, et al. 2019. *MNRAS* 483:5499–507
Kupriyanova EG, Melnikov VF, Puzynya VM, Shibasaki K, Ji HS. 2014. *Astron. Rep.* 58:573–77
Kupriyanova EG, Ratcliffe H. 2016. *Adv. Space Res.* 57:1456–67
Kuznetsov AA, Van Doorsselaere T, Reznikova VE. 2015. *Solar Phys.* 290:1173–94
Li D, Ning ZJ, Huang Y, et al. 2017. *Ap. J.* 849:113
Liu W, Ofman L. 2014. *Solar Phys.* 289:3233–77

Liu W, Title AM, Zhao J, et al. 2011. *Ap. J. Lett.* 736:L13
Long DM, Bloomfield DS, Chen PF, et al. 2017. *Solar Phys.* 292:7
Lopin I, Nagorny I. 2015. *Ap. J.* 810:87
Lopin I, Nagorny I. 2019. *MNRAS* 488:660–75
Luna M, Terradas J, Oliver R, Ballester JL. 2010. *Ap. J.* 716:1371–80
Magyar N, Van Doorsselaere T. 2016. *Astron. Astrophys.* 595:A81
Mandal S, Magyar N, Yuan D, Van Doorsselaere T, Banerjee D. 2016a. *Ap. J.* 820:13
Mandal S, Yuan D, Fang X, et al. 2016b. *Ap. J.* 828:72
Mariska JT. 2006. *Ap. J.* 639:484–94
Mariska JT, Muglach K. 2010. *Ap. J.* 713:573–83
Marsh MS, De Moortel I, Walsh RW. 2011. *Ap. J.* 734:81
Marsh MS, Walsh RW. 2009. *Ap. J. Lett.* 706:L76–79
Marsh MS, Walsh RW, Plunkett S. 2009. *Ap. J.* 697:1674–80
Melnikov VF, Reznikova VE, Shibasaki K, Nakariakov VM. 2005. *Astron. Astrophys.* 439:727–36
Mészárosová H, Karlický M, Rybák J, Jiřička K. 2009. *Ap. J. Lett.* 697:L108–10
Mészárosová H, Rybák J, Kashapova L, et al. 2016. *Astron. Astrophys.* 593:A80
Moon YJ, Choe GS, Park YD, et al. 2002. *Ap. J.* 574:434–39
Morton RJ, Tomczyk S, Pinto RF. 2016. *Ap. J.* 828:89
Nakariakov VM, Afanasyev AN, Kumar S, Moon YJ. 2017. *Ap. J.* 849:62
Nakariakov VM, Anfinogentov SA, Nisticò G, Lee DH. 2016a. *Astron. Astrophys.* 591:L5
Nakariakov VM, Erdélyi R. 2009. *Space Sci. Rev.* 149:1–2
Nakariakov VM, Foullon C, Verwichte E, Young NP. 2006. *Astron. Astrophys.* 452:343–46
Nakariakov VM, Hornsey C, Melnikov VF. 2012. *Ap. J.* 761:134
Nakariakov VM, Kolotkov DY, Kupriyanova EG, et al. 2019a. *Plasma Phys. Control. Fusion* 61:014024
Nakariakov VM, Kosak MK, Kolotkov DY, et al. 2019b. *Ap. J. Lett.* 874:L1
Nakariakov VM, Ofman L. 2001. *Astron. Astrophys.* 372:L53–56
Nakariakov VM, Pilipenko V, Heilig B, et al. 2016b. *Space Sci. Rev.* 200:75–203
Nakariakov VM, Verwichte E. 2005. *Living Rev. Solar Phys.* 2:3
Nakariakov VM, Zimovets IV. 2011. *Ap. J. Lett.* 730:L27
Nechaeva A, Zimovets IV, Nakariakov VM, Goddard CR. 2019. *Ap. J. Suppl. Ser.* 241:31
Nisticò G, Nakariakov VM, Verwichte E. 2013. *Astron. Astrophys.* 552:A57
Nisticò G, Pascoe DJ, Nakariakov VM. 2014. *Astron. Astrophys.* 569:A12
Ofman L. 2007. *Ap. J.* 655:1134–41
Ofman L. 2016. *AGU Geophys. Monogr. Ser.* 216:241–52
Ofman L, Aschwanden MJ. 2002. *Ap. J. Lett.* 576:L153–56
Ofman L, Liu W. 2018. *Ap. J.* 860:54
Ofman L, Liu W, Title A, Aschwanden M. 2011. *Ap. J. Lett.* 740:L33
Ofman L, Wang T. 2002. *Ap. J. Lett.* 580:L85–88
Ofman L, Wang TJ, Davila JM. 2012. *Ap. J.* 754:111
Ogrodowczyk R, Murawski K, Solanki SK. 2009. *Astron. Astrophys.* 495:313–18
Oliver R, Ruderman MS, Terradas J. 2015. *Ap. J.* 806:56
Owen NR, De Moortel I, Hood AW. 2009. *Astron. Astrophys.* 494:339–53
Pant V, Tiwari A, Yuan D, Banerjee D. 2017. *Ap. J.* 847:L5
Pascoe DJ, Anfinogentov SA, Goddard CR, Nakariakov VM. 2018. *Ap. J.* 860:31
Pascoe DJ, Goddard CR, Nakariakov VM. 2017. *Ap. J. Lett.* 847:L21
Pascoe DJ, Goddard CR, Nisticò G, Anfinogentov S, Nakariakov VM. 2016a. *Astron. Astrophys.* 589:A136
Pascoe DJ, Goddard CR, Nisticò G, Anfinogentov S, Nakariakov VM. 2016b. *Astron. Astrophys.* 585:L6
Pascoe DJ, Hood AW, De Moortel I, Wright AN. 2013a. *Astron. Astrophys.* 551:A40
Pascoe DJ, Hood AW, Van Doorsselaere T. 2019. *Front. Astron. Space Sci.* 6:22
Pascoe DJ, Nakariakov VM. 2016. *Astron. Astrophys.* 593:A52
Pascoe DJ, Nakariakov VM, Arber TD, Murawski K. 2009. *Astron. Astrophys.* 494:1119–25
Pascoe DJ, Nakariakov VM, Kupriyanova EG. 2013b. *Astron. Astrophys.* 560:A97

Pascoe DJ, Wright AN, De Moortel I. 2011. *Ap. J.* 731:73
Peter H. 2015. *Philos. Trans. R. Soc. Lond. Ser. A* 373:20150055
Porter LJ, Klimchuk JA, Sturrock PA. 1994. *Ap. J.* 435:482–501
Provornikova E, Ofman L, Wang T. 2018. *Adv. Space Res.* 61:645–54
Pugh CE, Armstrong DJ, Nakariakov VM, Broomhall AM. 2016. *MNRAS* 459:3659–76
Reale F. 2014. *Living Rev. Solar Phys.* 11:4
Reale F. 2016. *Ap. J. Lett.* 826:L20
Reale F, Lopez-Santiago J, Flaccomio E, Petralia A, Sciortino S. 2018. *Ap. J.* 856:51
Reznikova VE, Shibasaki K. 2011. *Astron. Astrophys.* 525:A112
Roberts B. 2000. *Solar Phys.* 193:139–52
Roberts B, Edwin PM, Benz AO. 1984. *Ap. J.* 279:857–65
Ruderman MS. 2013. *Astron. Astrophys.* 553:A23
Ruderman MS, Petrukhin NS, Pelinovsky E. 2016. *Solar Phys.* 291:1143–57
Russell AJB, Simões PJA, Fletcher L. 2015. *Astron. Astrophys.* 581:A8
Selwa M, Murawski K, Solanki SK. 2005. *Astron. Astrophys.* 436:701–9
Simões PJA, Fletcher L, Hudson HS, Russell AJB. 2013. *Ap. J.* 777:152
Soler R, Luna M. 2015. *Astron. Astrophys.* 582:A120
Srivastava AK, Lalitha S, Pandey JC. 2013. *Ap. J. Lett.* 778:L28
Su JT, Liu Y, Liu S, et al. 2013. *Ap. J.* 762:42
Tan B, Yu Z, Huang J, Tan C, Zhang Y. 2016. *Ap. J.* 833:206
Taroyan Y, Erdélyi R, Doyle JG, Bradshaw SJ. 2005. *Astron. Astrophys.* 438:713–20
Terradas J. 2009. *Space Sci. Rev.* 149:255–82
Terradas J, Andries J, Goossens M, et al. 2008a. *Ap. J. Lett.* 687:L115–18
Terradas J, Arregui I, Oliver R, et al. 2008b. *Ap. J.* 679:1611–20
Tian H, McIntosh SW, Habbal SR, He J. 2011. *Ap. J.* 736:130
Tian H, McIntosh SW, Wang T, et al. 2012. *Ap. J.* 759:144
Tian H, Young PR, Reeves KK, et al. 2016. *Ap. J. Lett.* 823:L16
Tomczyk S, McIntosh SW. 2009. *Ap. J.* 697:1384–91
Tsiklauri D, Nakariakov VM, Arber TD, Aschwanden MJ. 2004. *Astron. Astrophys.* 422:351–55
Uritsky VM, Davila JM, Viall NM, Ofman L. 2013. *Ap. J.* 778:26
Van Doorsselaere T, Antolin P, Yuan D, Reznikova V, Magyar N. 2016. *Front. Astron. Space Sci.* 3:4
Van Doorsselaere T, De Groof A, Zender J, Berghmans D, Goossens M. 2011a. *Ap. J.* 740:90
Van Doorsselaere T, Kupriyanova EG, Yuan D. 2016. *Solar Phys.* 291:3143–64
Van Doorsselaere T, Verwichte E, Terradas J. 2009. *Space Sci. Rev.* 149:299–324
Van Doorsselaere T, Wardle N, Del Zanna G, et al. 2011b. *Ap. J.* 727:L32
Vasheghani Farahani S, Hornsey C, Van Doorsselaere T, Goossens M. 2014. *Ap. J.* 781:92
Verth G, Erdélyi R. 2008. *Astron. Astrophys.* 486:1015–22
Verwichte E, Haynes M, Arber TD, Brady CS. 2008. *Ap. J.* 685:1286–90
Verwichte E, Marsh M, Foullon C, et al. 2010. *Ap. J. Lett.* 724:L194–98
Verwichte E, Van Doorsselaere T, Foullon C, White RS. 2013. *Ap. J.* 767:16
Wang T. 2011. *Space Sci. Rev.* 158:397–419
Wang T, Innes DE, Qiu J. 2007. *Ap. J.* 656:598–609
Wang T, Ofman L, Davila JM. 2013. *Ap. J. Lett.* 775:L23
Wang T, Ofman L, Davila JM, Su Y. 2012. *Ap. J. Lett.* 751:L27
Wang T, Ofman L, Sun X, Provornikova E, Davila JM. 2015. *Ap. J. Lett.* 811:L13
Wang T, Ofman L, Sun X, Solanki SK, Davila JM. 2018. *Ap. J.* 860:107
Wang TJ. 2016. *AGU Geophys. Monogr. Ser.* 216:395–418
Wang YM. 2009. *Space Sci. Rev.* 144:383–99
Yu S, Nakariakov VM, Selzer LA, Tan B, Yan Y. 2013. *Ap. J.* 777:159
Yuan D, Nakariakov VM. 2012. *Astron. Astrophys.* 543:A9
Yuan D, Nakariakov VM, Chorley N, Foullon C. 2011. *Astron. Astrophys.* 533:A116
Yuan D, Shen Y, Liu Y, et al. 2013. *Astron. Astrophys.* 554:A144

Yuan D, Van Doorsselaere T. 2016. *Ap. J. Suppl. Ser.* 223:23
Yuan D, Van Doorsselaere T, Banerjee D, Antolin P. 2015. *Ap. J.* 807:98
Zaitsev VV, Stepanov AV. 1989. *Sov. Astron. Lett.* 15:66–68
Zajtsev VV, Stepanov AV. 1975. *Issled. Geomagn. Aeron. Fiz. Solntsa* 37:3–10
Zavershinskii DI, Kolotkov DY, Nakariakov VM, Molevich NE, Ryashchikov DS. 2019. *Phys. Plasmas* 26:082113
Zhang Y, Zhang J, Wang J, Nakariakov VM. 2015. *Astron. Astrophys.* 581:A78
Zhugzhda YD. 1996. *Phys. Plasmas* 3:10–21
Zimovets IV, Nakariakov VM. 2015. *Astron. Astrophys.* 577:A4

Annual Review of Astronomy and Astrophysics

Volume 58, 2020

Contents

Indexes

Errata

An online log of corrections to *Annual Review of Astronomy and Astrophysics* articles may be found at http://www.annualreviews.org/errata/astro